RSC Advances

PAPER

View Article Online
View Journal | View Issue

Cite this: *RSC Adv.*, 2025, **15**, 37226

Synthesis and characterization of fluorescent magnetic nanoparticles: a dual-function platform for DNA separation and real-time visualization

Md. Shamiull Alim Munna, [a] Md. Mazharul Islam, [a] Mohammad Ahasanur Rabbi, [b] O. Thompson Mefford, [c] Alexander Malaj,[c] Md. Shahidul Islam,[a] Hasan Ahmad [a] and Md. Mahbubor Rahman *[a]

Multifunctional magnetic nanoparticles have become the subject of significant attention in biomedical applications recently, especially for their applications in the separation and detection of biomolecules. This study focuses on the preparation of dual-functional iron oxide magnetic nanoparticles (Fe_3O_4 MNPs) conjugated with a fluorescent dye for facilitating real-time tracing and visualization of DNA molecules during a separation process. The fluorescent Fe_3O_4@SiO_2@FITC nanoparticles were used both for the separation of DNA molecules from a solution by applying an external magnetic field and for quantification by analyzing the fluorescence properties of the nanoparticles upon DNA binding. The pH of the solution was optimized to achieve the best adsorption efficiency using the proposed method. Approximately 91% adsorption efficiency was achieved using fluorescent Fe_3O_4@SiO_2@FITC MNPs at a pH of 4.44 with a recovery of ~50% at the same pH, while amine functionalized Fe_3O_4@SiO_2-NH_2 MNPs exhibited lower adsorption efficiencies at every pH of the medium (maximum ~89% at a pH of 4.44 and minimum ~52% at a pH of 11.01). The ultraviolet-visible (UV-Vis) and fluorescence emission spectra showed that the increasing number of DNA molecules adsorbed on the Fe_3O_4@SiO_2@FITC MNPs led to a gradual decrease in the absorption and fluorescence emission intensity, indicating the presence of DNA molecules. This study highlights the potential of fluorescent MNPs as a dual-function platform, combining magnetic separation and fluorescence-based real time monitoring of DNA.

Received 27th June 2025
Accepted 22nd September 2025

DOI: 10.1039/d5ra04563k

rsc.li/rsc-advances

1 Introduction

Advancing molecular diagnosis requires efficient, rapid, and high-throughput methodologies for the extraction of such biomolecules in their purified forms as proteins, DNAs, antibodies, and antigens from suspended solutions.[1–4] One widely accepted method currently used involves the application of magnetic nanoparticles (MNPs), which exhibit unique properties such as superparamagnetism,[5] biocompatibility[6] and large surface to volume ratios.[7] Their magnetic properties, coupled with suitable functional groups, make them potential candidates for efficient and selective isolation of biomolecules. For example, anti-immunoglobulin-coated MNPs have been used to isolate proteins expressed in cellular extracts[8] and dendron-coated MNPs exhibited 100% retention capability for proteins under acidic conditions.[9] Specific targeting can also be achieved by the conjugation of specifically tagged antibodies, antigens, or other biomolecules on the nanoparticles. For example, immunospecific MNPs have been successfully designed to isolate red blood cells, bacteria, lung cancer cells, and breast cancer cells,[10] while sulfanilamide modified MNPs have been used for the purification of the carbonic anhydrase enzyme[11] and antibody-conjugated MNPs have been effectively used for selective isolation of the expressed recombinant hepatitis B surface antigen (rHBsAg) in yeast pichia pastoris.[12]

Magnetic isolation of DNA from complex biological samples enhances operational efficiency, selectivity, and capacity, outperforming conventional methods such as chromatographic,[13] solvent extraction,[14] ion exchange[15] and salting-out methods,[16] all of which are labor-intensive and involve hazardous chemicals as well as the need for specialized equipment.[17] In contrast, magnetic nanoparticle-based systems streamline the process, enabling high-throughput and eco-friendly protocols.[18]

Over the last 50 years, iron oxide nanoparticles (IONPs) have garnered significant attention in this area of biomedical research, particularly for their applications in DNA separation and purification.[19,20] Core–shell Fe_3O_4 nanoparticles, which are coated with silica and functionalized with chitosan, facilitate easy separation of DNA while also enhancing its binding affinity. Optimization studies have demonstrated that these

[a]*Polymer Colloids and Nanomaterials (PCN) Group, Department of Chemistry, Rajshahi University, Rajshahi 6205, Bangladesh. E-mail: mrchem@ru.ac.bd*

[b]*BCSIR Rajshahi, Rajshahi 6205, Bangladesh*

[c]*Department of Materials Science and Engineering, Clemson University, Clemson, South Carolina 29634, USA*

nanoparticles achieve an impressive adsorption efficiency of approximately 88% and an elution efficiency nearing 98%.[21] A second strategy utilizes polyethyleneimine (PEI)-functionalized IONPs for capturing both plasmid and genomic DNA, an approach which not only facilitates robust DNA binding but also enables efficient magnetofection processes.[22] In addition, because amine functionalized IONPs can form strong ionic interactions with the negatively charged phosphate backbone of DNA in acidic pH, amine functionalized magnetic IONPs have proven to be advantageous in the isolation of DNA.[23–25] Furthermore, the adsorption characteristics of DNA on bare IONPs have been explored in the detection of arsenate as its ionic displacement of adsorbed DNA leads to measurable fluorescence changes.[26] However, despite their potential, detection and quantification of DNA molecules using MNPs remain difficult due to such complex issues as their lack of optical properties, limitations that could potentially be addressed by novel fluorescent iron oxide MNPs.

Non-fluorescence quantification techniques, such as spectrophotometric methods, are widely used for estimating DNA concentration and purity by measuring absorbance at specific wavelengths. DNA absorbs ultraviolet (UV) light at 260 nm, allowing for rapid quantification.[27] However, these methods lack the ability to distinguish between DNA, RNA, and protein contamination, leading to low specificity. Additionally, their sensitivity is limited, making it challenging to accurately measure low DNA concentrations, particularly in dilute or degraded samples.[28,29] Gel-based methods, such as agarose gel electrophoresis, provide a visual means of assessing DNA concentration and integrity. While this method offers an additional advantage of simultaneously assessing DNA integrity, it is semi-quantitative at best as factors such as dye-binding efficiency, gel composition, and electrophoresis conditions can influence accuracy.[30,31] Moreover, its sensitivity and specificity are lower than those of the more advanced quantification methods.[32,33] In contrast, polymerase chain reaction (PCR) based quantification, including quantitative PCR (qPCR) and digital PCR (dPCR), provides exceptional sensitivity and specificity by amplifying target DNA sequences in real time. These methods enable absolute or relative DNA quantification with high precision even at extremely low concentrations.[34] However, PCR-based techniques require a highly specialized laboratory setup, expensive reagents, and careful optimization to ensure accurate and reproducible results.[35] Therefore, an alternative method for easy, fast and precise detection and quantification of DNA is required to address the current limitations.

The study reported here explores the synthesis of fluorescent MNPs for easy detection and quantification of DNA using UV-Vis spectrophotometry and fluorescence spectrophotometry. By integrating fluorescent molecules, these nanoparticles not only facilitate efficient DNA isolation through magnetic separation but also enable real-time visualization and tracking during the process. This dual functionality enhances their applicability in molecular biology and clinical diagnostics, where accuracy and efficiency are paramount. This study also explores the synthesis process, detailing the chemical and physical modifications of the nanoparticles required to impart magnetic and fluorescent properties. Additionally, the

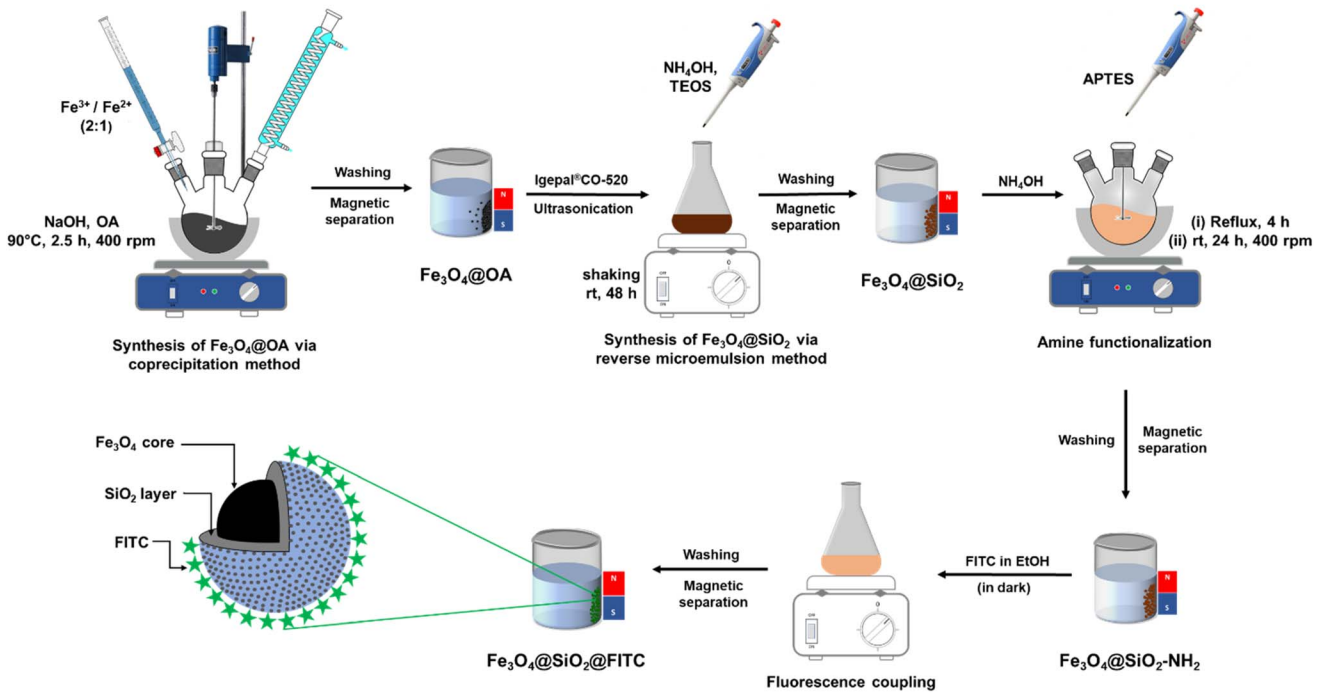

Scheme 1 Schematic illustration of the reaction setup for synthesizing FITC-conjugated iron oxide magnetic nanoparticles, *i.e.* Fe_3O_4@SiO_2@FITC MNPs, beginning with oleic acid coated iron oxide magnetic nanoparticles, *i.e.* Fe_3O_4@OA MNPs.

performance of nanoparticles in DNA separation, with special emphasis on their binding efficiency, specificity, and recovery rates, was also investigated.

2 Results and discussion

2.1 Synthesis and characterization of fluorescence MNPs

IONPs were synthesized following the conventional method for coprecipitation of iron salts outlined in the Experimental section. The structural characterization and surface functionalization of nearly monodispersed IONPs, initially coated with oleic acid (OA), was determined. Then, Fe_3O_4@OA MNPs were encapsulated with a silica (SiO_2) shell *via* reverse microemulsion followed by amine-functionalization. Finally, Fe_3O_4@SiO_2-NH_2 MNPs were conjugated with fluorescent isothiocyanate (FITC). The detailed synthesis procedure for the preparation of fluorescent iron oxide MNPs, *i.e.* Fe_3O_4@SiO_2@FITC MNPs, is schematically illustrated in Scheme 1.

Transmission electron microscopy (TEM) was used to assess the morphology and size distribution of the synthesized nanoparticles. As shown in Fig. 1a and b, typical TEM micrographs revealed nearly monodispersed Fe_3O_4 MNPs coated with oleic acid (OA), synthesized *via* co-precipitation. The nanoparticles exhibited uniform size distribution with a mean diameter of approximately 7.3 ± 0.2 nm (as shown in the histogram in Fig. 1c) and several morphologies including irregular cubic, spherical, and octahedral shapes. These particles demonstrated excellent dispersion in nonpolar solvents such as cyclohexane, affirming their colloidal stability. Dynamic Light Scattering (DLS) measurements for oleic acid-coated iron oxide magnetic nanoparticles (Fe_3O_4@OA) dispersed in cyclohexane (Fig. S4). The intensity-weighted hydrodynamic diameter was found to be 604.3 ± 174.6 nm, corresponding to a polydispersity index (PDI) of 0.084, indicating that the nanoparticles form secondary aggregates in the nonpolar medium. The relatively broad size distribution reflects polydispersity arising from hydrophobic interactions between oleyl chains, which promote cluster formation. These results confirm that while the primary nanoparticles are nanometer-sized (as shown in TEM), they exist as larger, colloidally stable assemblies in cyclohexane. Subsequent encapsulation of Fe_3O_4 within a silica matrix *via* reverse microemulsion method was confirmed by the TEM micrographs shown in Fig. 1d and e, where dark Fe_3O_4 cores are clearly embedded within a less dark SiO_2 shell. The aggregation observed in these micrographs was likely a result of drying

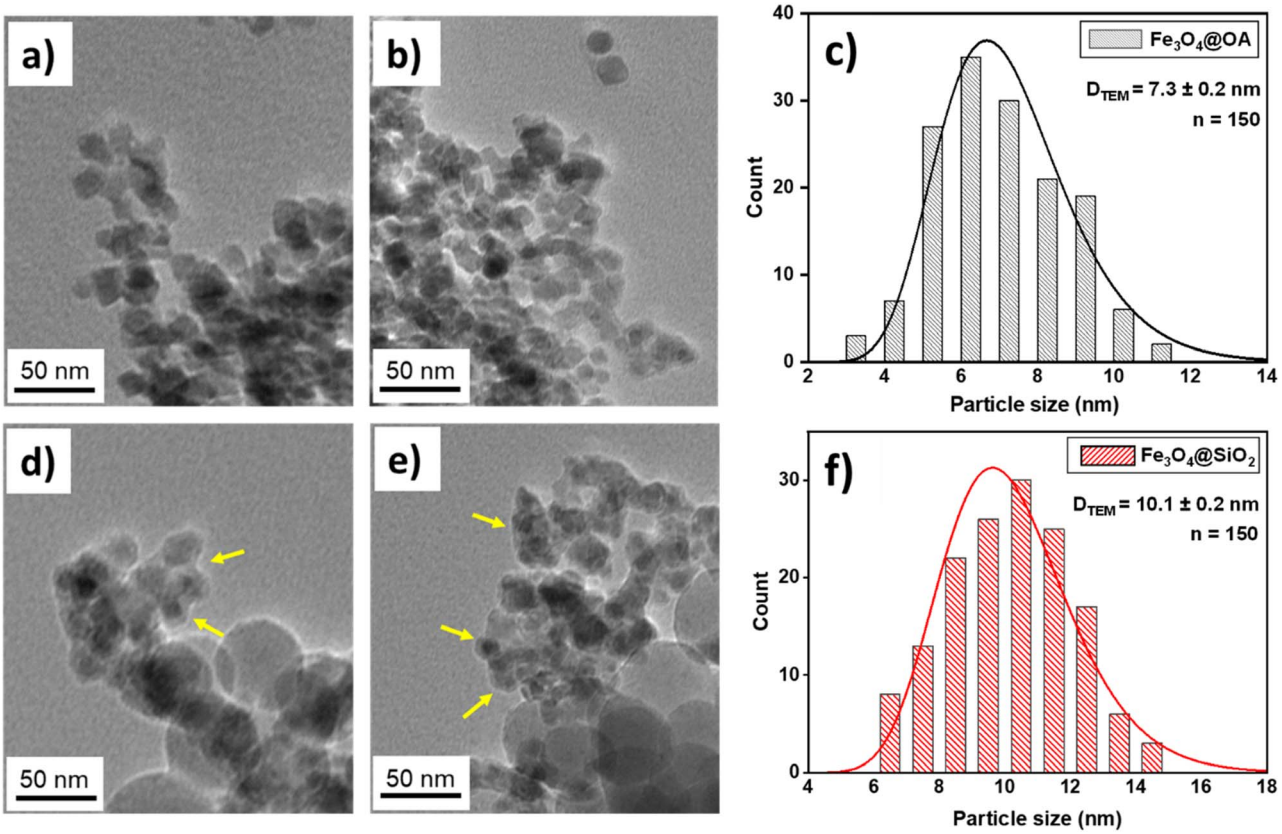

Fig. 1 (a and b) TEM images of oleic acid coated iron oxide magnetic nanoparticles, *i.e.* Fe_3O_4@OA MNPs, showing nearly monodispersed, cubic-shaped nanoparticles in an aggregated form with 50 nm scale bars. (c) Histogram showing the corresponding particle size distribution of Fe_3O_4@OA MNPs. (d and e) TEM images of silica coated iron oxide magnetic nanoparticles, *i.e.* Fe_3O_4@SiO_2 MNPs, in an aggregated form with 50 nm scale bars. Yellow arrows signify the silica layer around the MNPs. (f) Histogram showing the corresponding particle size distribution of Fe_3O_4@SiO_2 MNPs. The solid lines are the best-fit of the data using a log-normal distribution function. Aggregation is due to the drying of the solvent, resulting in the MNPs moving closer together during sample preparation.

during sample preparation. The silica-coated magnetic nanoparticles (*i.e.* Fe_3O_4@SiO_2 MNPs) displayed a slightly increased average diameter of 10.1 ± 0.2 nm (as shown in the histogram in Fig. 1f) and a more aggregated and irregular morphology compared to their uncoated counterparts.

Powder X-ray diffraction (XRD) analysis provided insights into the crystalline nature of the materials. As depicted in Fig. 2a, the Fe_3O_4@OA MNPs showed distinct diffraction peaks at 2θ values of 30.1°, 35.5°, 43.1°, 53.5°, 57.0°, 62.6°, and 74.2°, corresponding to the (220), (311), (400), (422), (511), (440), and (533) planes, respectively. These peaks are in good agreement with the standard ones reported by the JCPDS (magnetite, PDF No. 19-0629), confirming a cubic inverse spinel structure.[36] The average crystallite size of 0.08 ± 0.15 nm was calculated using the Scherrer equation, $D = k\lambda/B\cos\theta$,[37] a result which is aligned with TEM observations. In contrast, the XRD structures of Fe_3O_4@SiO_2 MNPs exhibited a broad hump between 19° and 27°, characteristic of amorphous silica, with no additional crystalline peaks except the reduced intensity of the Fe_3O_4 reflections, supporting successful silica encapsulation.

The magnetic properties of both Fe_3O_4@OA MNPs and Fe_3O_4@SiO_2 MNPs were evaluated *via* magnetization (emu g^{-1}) *versus* applied field (Oe) measurements at ambient conditions. As shown in Fig. 2b, both samples exhibited superparamagnetic behavior with negligible remanence and coercivity, indicating their single-domain nature. Notably, the saturation magnetization (M_S) of Fe_3O_4@OA MNPs was found to be ~58.8 emu g^{-1}, while that of Fe_3O_4@SiO_2 MNPs dropped to ~16.3 emu g^{-1} due to the presence of the nonmagnetic silica shell. Nevertheless, the coated nanoparticles retained sufficient magnetic responsiveness, providing them suitable for magnetic targeting applications.

The surface chemistry and successful amine functionalization were confirmed by zeta potential measurements conducted over a range of pH values. The amine functionalized silica coated iron oxide magnetic nanoparticles, *i.e.* Fe_3O_4@SiO_2-NH_2 MMPs, exhibited a positive surface charge at acidic pH values, with zeta potentials of +22.1 mV and +18.9 mV at pH 2.10 and 4.20, respectively. This positive charge results from the protonation of amine groups in an acidic media as illustrated in Fig. 3b. The isoelectric point (IEP) was found to be pH 5.55 as shown in Fig. 3a, beyond which the nanoparticles showed signs of aggregation due to deprotonation and reduced electrostatic repulsion. Though, the colloidal stability of the nanocomposites was maintained between pH 2 and pH 5.

Further confirmation of surface functional groups was obtained through Fourier-transform infrared (FTIR) spectroscopy. Fig. S1(a and b) shows the FTIR spectra of Fe_3O_4@OA MNPs and Fe_3O_4@SiO_2 MNPs. Characteristic O–H stretching vibrations appeared around 3400–3500 cm^{-1}, indicative of water molecule and silanol groups (Si–OH), the latter being primarily located at the surface of the silica coated nanoparticles. The bands between 1050 cm^{-1} and 1150 cm^{-1} represent the most significant spectral region, and the accompanying shoulders are attributed to the asymmetric stretching vibrations of Si–O–Si[38] and the Si–O–Si symmetric stretches observed in the 798.79 cm^{-1} region.[39] The bands at 2925.07 and 2852.12 cm^{-1} were attributed to the asymmetric and symmetric stretches of the CH_2 groups, confirming the presence of oleic acid.[40] The two bands appearing at approximately 1638.59 cm^{-1} and

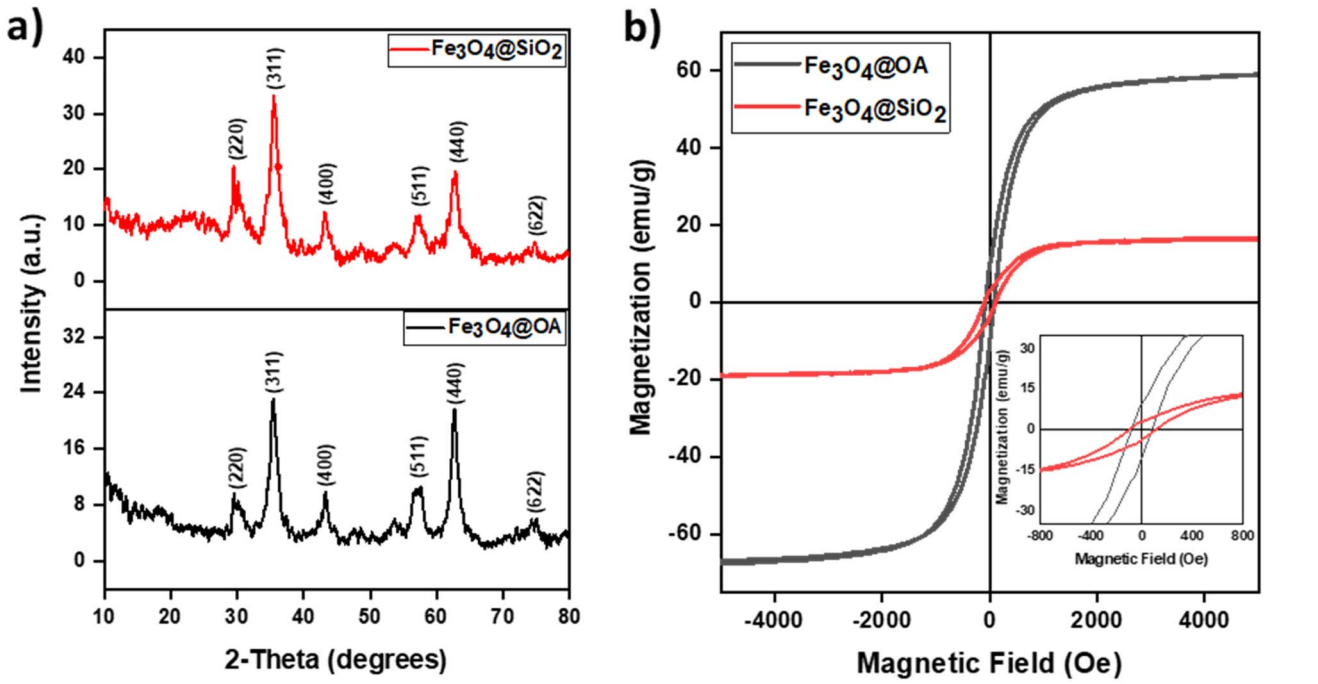

Fig. 2 (a) X-ray diffraction pattern for oleic acid coated iron oxide magnetic nanoparticles, *i.e.* Fe_3O_4@OA MNPs (black curve), and silica coated iron oxide magnetic nanoparticles, *i.e.* Fe_3O_4@SiO_2 MNPs (red curve). (b) The magnetization curves at 300 K for Fe_3O_4@OA MNPs (black curve) and Fe_3O_4@SiO_2 MNPs (red curve). Inset: zoomed-in view of magnetization curves at the low field region.

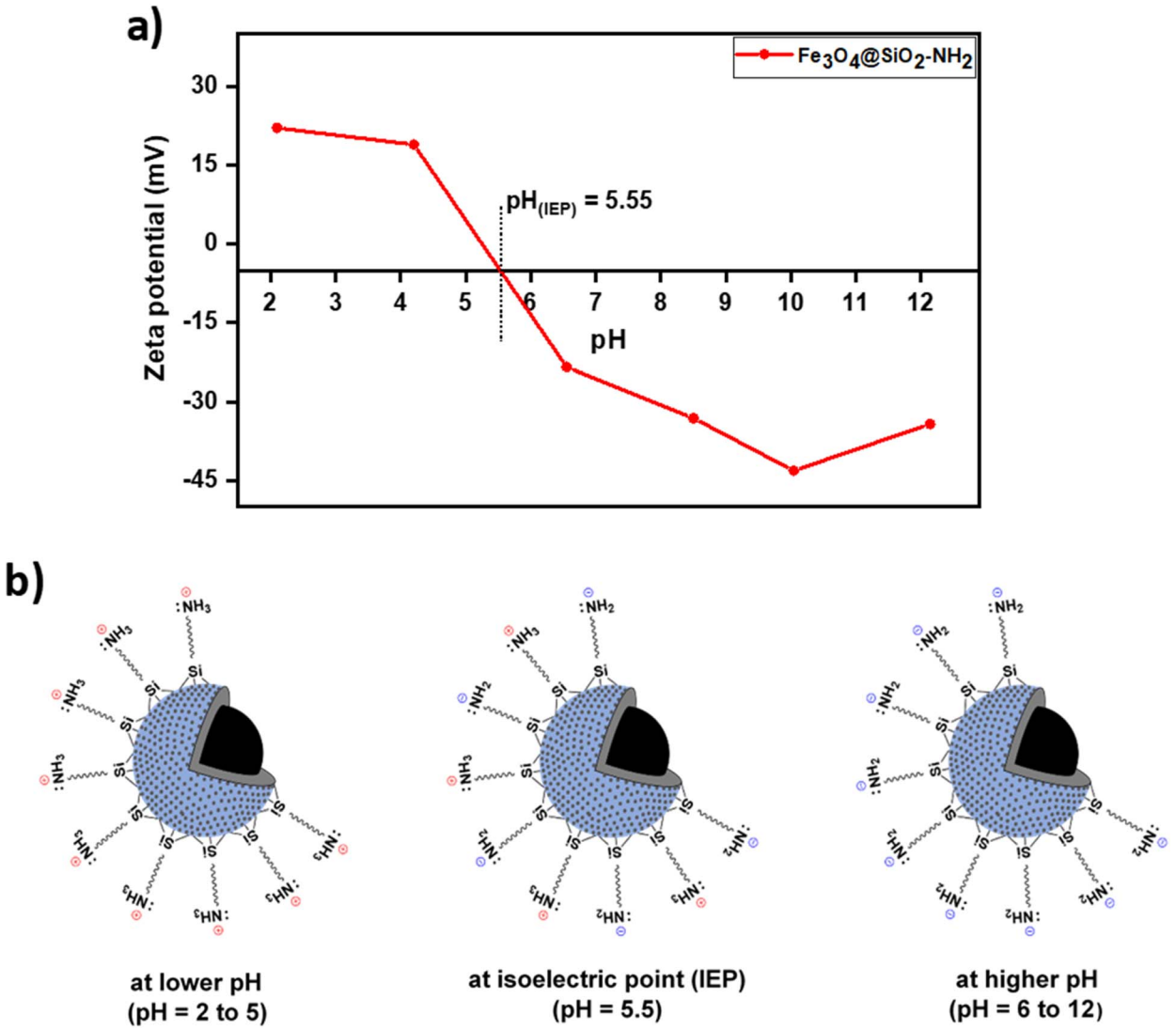

Fig. 3 (a) Zeta potential (ζ) as a function of pH for amine functionalized silica coated iron oxide magnetic nanoparticles, *i.e.* Fe_3O_4@SiO_2-NH_2 MNPs, in DI water. The isoelectric point (IEP) shows at pH = 5.55. (b) Illustration of colloidal systems and their surface charges at different pH values for Fe_3O_4@SiO_2-NH_2 MNPs in DI water.

1618.70 cm^{-1} were attributed to the asymmetric and the symmetric stretch of –COO– respectively. The presence of these bands results from the complexation between iron atoms and the carboxylate groups of oleic acid.[31–34] The presence of strong Fe–O vibrations around 610.74 cm^{-1} and 474.80 cm^{-1} further confirms the iron oxide core. The appearance of these bands at higher wave numbers indicates the interaction between –COO– groups of oleic acid and iron oxide nanoparticles.[41] After silica coating, the Fe–O bands diminished, consistent with successful encapsulation.

Field emission scanning electron microscopy (FE-SEM) combined with energy-dispersive X-ray spectroscopy (EDS) provides further morphological and elemental insights. As shown in Fig. S2(a and b), the surface of Fe_3O_4@OA MNPs appeared distorted and cubic, while the Fe_3O_4@SiO_2 MNPs adopted a more spherical and uniform morphology. EDS analysis (Fig. S3) confirmed the elemental composition of Fe_3O_4@OA MNPs (Fe, O, C) and Fe_3O_4@SiO_2 MNPs (Fe, O, Si, C), with reduced carbon content post-coating indicating the removal of excess oleic acid.

The amine functionalized magnetic nanoparticles were labelled with fluorescein isothiocyanate (FITC) for real time quantification of DNA molecules. The reaction between primary amine groups (–NH_2) and fluorescein isothiocyanate (FITC) molecules in the presence of ammonium hydroxide typically following a nucleophilic addition–elimination mechanism. This reaction results in the formation of a thiourea derivative, where the primary amine (–NH_2) reacts with the isothiocyanate group (–N=C=S) of FITC as illustrated in Scheme S1. Primarily, the lone pair electrons on the nitrogen atom of the primary amine (–NH_2) of Fe_3O_4@SiO_2-NH_2 attacks the electrophilic carbon atom of the isothiocyanate group, forming a tetrahedral intermediate. Then a proton is transferred within the intermediate, stabilizing the structure through the formation of a stable thiourea linkage (–NH–C=S–NH–R). This step is facilitated by the presence of ammonium hydroxide which acts

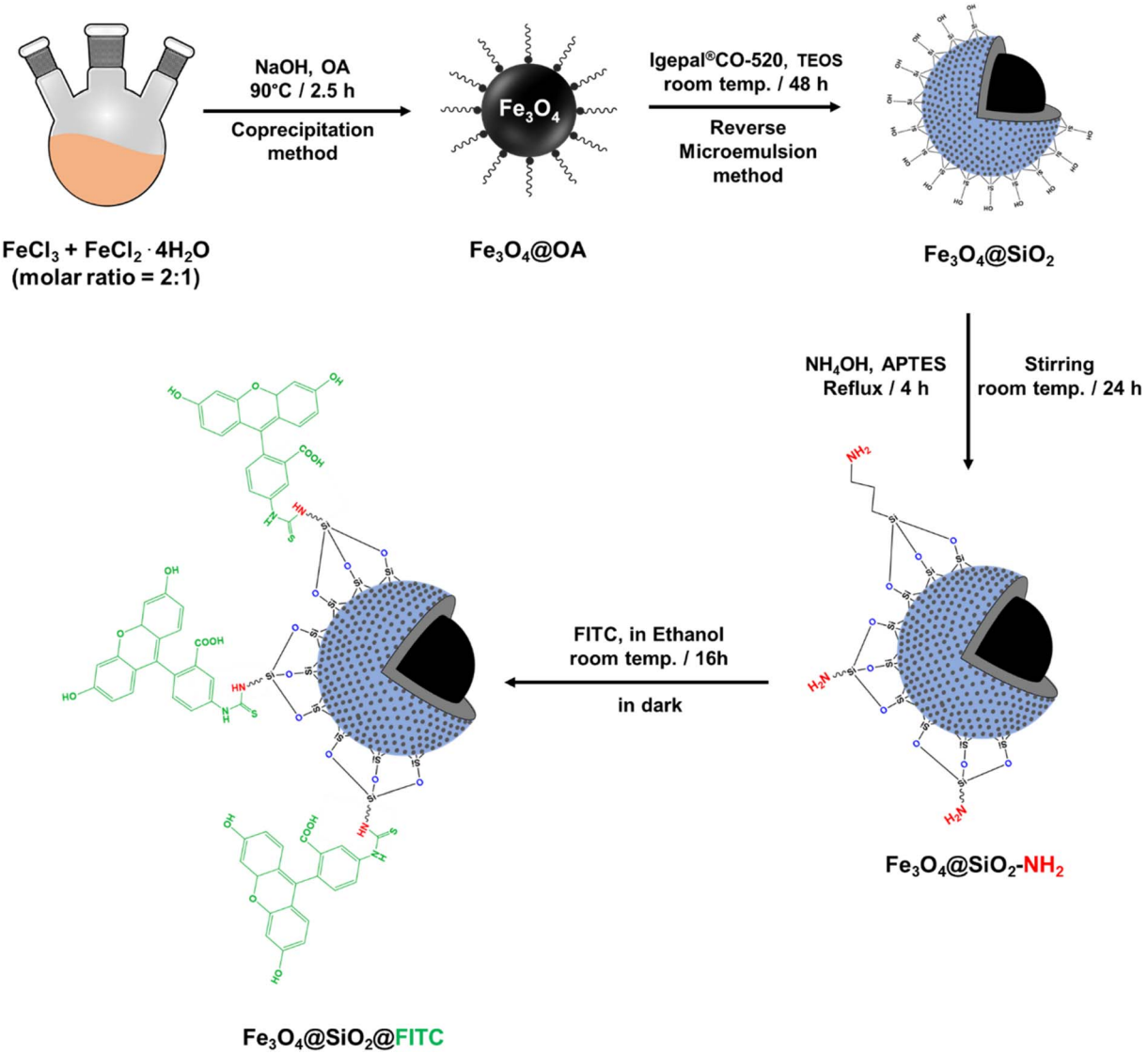

Scheme 2 Schematic representation of the synthesis pathway for FITC-conjugated iron oxide magnetic nanoparticles, *i.e.* Fe_3O_4@SiO_2@FITC MNPs, starting from oleic acid coated iron oxide magnetite nanoparticles, *i.e.* Fe_3O_4@OA MNPs.

as a mild base and can accept or donate protons. A schematic representation of the entire synthesis process is illustrated in Scheme 2.

In the UV-vis absorption spectra of Fe_3O_4@SiO_2-NH_2 MNPs shown in Fig. 4a, no absorbance peak is observed in the 400 nm to 650 nm range. This investigation found that FITC-labelled silica coated iron oxide magnetic nanoparticles, *i.e.* Fe_3O_4@SiO_2@FITC MNPs (green curve), show a maximum absorption, $\lambda_{(max)}$, at 494 nm in a phosphate buffer solution (PBS) at pH = 7.4 after extensive washing and magnetic separation, indicating the successful conjugations of FITC with amine functionalized silica coated iron oxide magnetic nanoparticles. The FITC (blue curve) exhibits the most dominant absorption peaks at a wavelength of 494 nm. Upon excitation by UV light, the delocalized π-electrons in its conjugated system are promoted from π-bonding orbitals to π-antibonding orbitals. On the other hand, Fe_3O_4@SiO_2@FITC MNPs showed an excitation peak at a lower wavelength of 490 nm, a result that can be attributed to the different transitions of such electrons as ligand to metal or metal to ligand. Furthermore, the interaction between FITC and iron oxide may involve charge transfer processes that can result in electronic transitions. In addition, the movement of electrons between iron oxide and FITC can lead to changes in the position of absorption peak.[42,43] A potential reaction mechanism for fluorescent coupling is illustrated in Scheme S1.

The absorption maxima of FITC-labeled nanoparticles were found to be pH-sensitive.[44,45] As the pH increased from acidic to basic, $\lambda_{(max)}$ shifted from 443 nm to 494 nm as shown in Fig. 4b, a shift that can be attributed to the deprotonation of the FITC phenolic (–OH) and carboxylic groups (–COOH), resulting in structural rearrangements and enhanced electron delocalization as illustrated in Scheme S2. In the neutral or slightly basic conditions, the FITC moiety seemed to be negatively charged as a result of the deprotonation of the phenolic group. As the pH

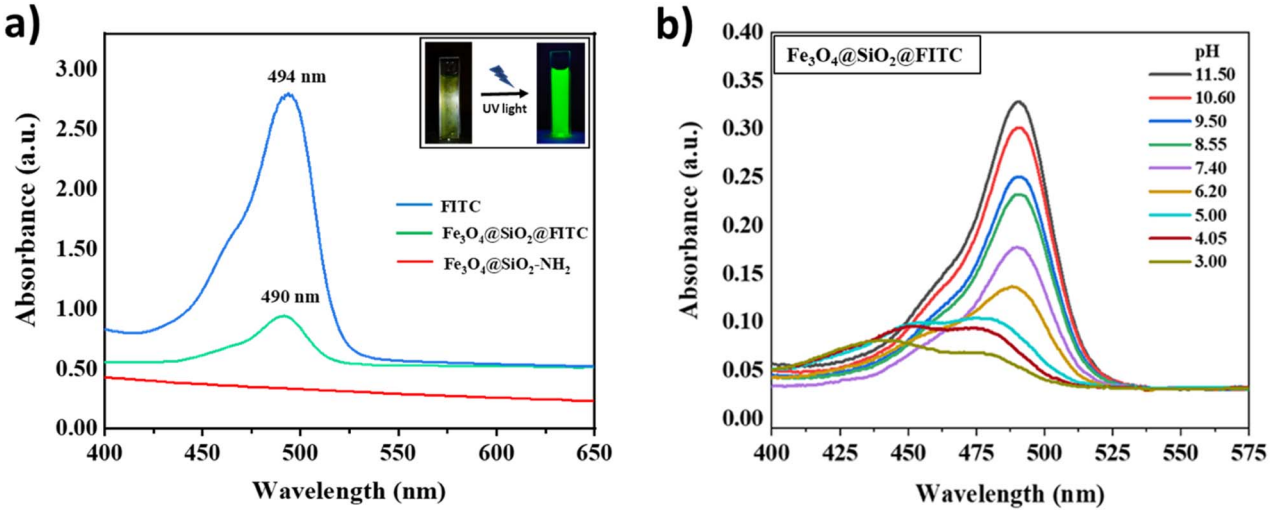

Fig. 4 (a) UV-Vis absorption spectra of amine functionalized silica coated iron oxide magnetic nanoparticles, *i.e.* Fe_3O_4@SiO_2-NH_2 MNPs (red curve), FITC labelled silica coated iron oxide magnetic nanoparticles, *i.e.* Fe_3O_4@SiO_2@FITC MNPs (green curve), and free FITC (blue curve) at pH 7.40 in phosphate buffer solution (PBS). Inset shows the bright green light emission upon excitation by UV light and in the absence of UV light. (b) UV-Vis absorption spectra of FITC labelled silica coated iron oxide magnetic nanoparticles, *i.e.* Fe_3O_4@SiO_2@FITC MNPs, at various pH in PBS.

increases in the basic region, more deprotonations occur, and the carboxylate anion ($-COO^-$) forms a new ring with the fluorescein core. As a result of ionization and ring formation, delocalized electrons cause a rapid increase in absorption intensity. The dynamic behavior of FITC in response to pH highlights its potential in biosensing and fluorescence-based diagnostics.[46]

2.2 Magnetic separation of DNA

2.2.1 Effect of pH. Depending on the pH of the dispersion media, the Fe_3O_4@SiO_2-NH_2 MNPs, exhibit fluctuation in net surface charge as they contained amine ($-NH_2$) groups as illustrated in Fig. 3b. The objective of this investigation was to determine how the pH of the medium influenced DNA adsorption and desorption. In the lower pH range, the surface amine group of the magnetic nanoparticles can be protonated as $-NH_3^+$. Fig. 5a shows that a higher percentage of DNA adsorption, approximately 89% of that added, was observed at pH 4.44; the amount decreased as the pH increased, reaching a minimum of approximately 52% of the added DNA at pH 11.01 regardless of temperature. Because of the deprotonation of the cationic amine ($-NH_3^+$), which is the primary group that

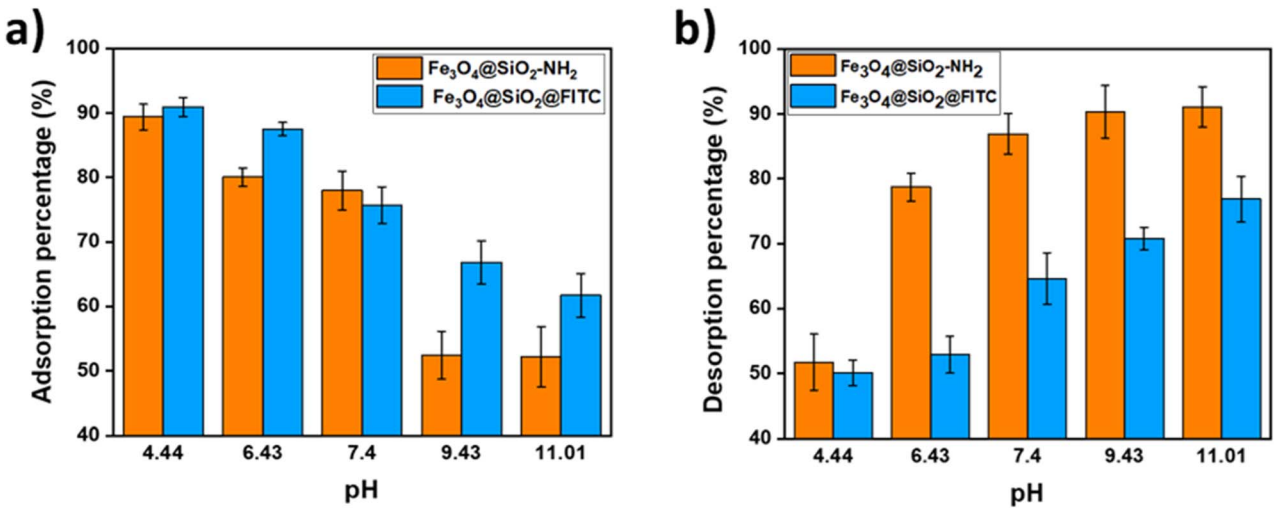

Fig. 5 (a) DNA adsorption percentages for amine functionalized silica coated iron oxide nanoparticles, *i.e.* Fe_3O_4@SiO_2-NH_2 MNPs, and FITC-conjugated silica coated iron oxide nanoparticles, *i.e.* Fe_3O_4@SiO_2@FITC MNPs, at different pH values (5 mM ionic strength of phosphate buffer solution, 25 °C temperature, 30 min incubation time, and 1000 rpm). (b) DNA desorption percentages for Fe_3O_4@SiO_2-NH_2 MNPs and Fe_3O_4@SiO_2@FITC MNPs at different pH values (5 mM ionic strength of phosphate buffer solution, 40 °C temperature, 45 min incubation time, and 1000 rpm).

Table 1 The experimental values of DNA adsorption efficiency (%) of amine functionalized silica coated iron oxide magnetic nanoparticles, *i.e.* Fe_3O_4@SiO_2-NH_2 MNPs, and FITC conjugated iron oxide magnetic nanoparticles, *i.e.* Fe_3O_4@SiO_2@FITC MNPs, at different pH values

pH	DNA adsorption efficiency of Fe_3O_4@SiO_2-NH_2 MNPs (%)	DNA adsorption efficiency of Fe_3O_4@SiO_2@FITC MNPs (%)
4.44	89.41 ± 2.02	90.97 ± 1.48
6.43	80.06 ± 1.41	87.54 ± 1.02
7.40	77.97 ± 3.02	75.73 ± 2.84
9.43	52.44 ± 3.73	66.87 ± 3.31
11.01	52.21 ± 4.68	61.73 ± 3.38

attracts DNA onto the particle surface, the low adsorption of DNA was achieved at pH 11.01. However, when the magnetic particles have a net zero charge at the IEP, there is a balance between the negative and positive surface charges of the magnetic seed, possibly causing an interaction between the DNA and the nanoparticles due to hydrogen bonding.[25] It can, thus, be inferred that the pH-regulated protonated amine group is primarily useful for drawing DNA to the magnetic nanoparticles. The experimental values of the DNA adsorption efficiency of Fe_3O_4@SiO_2-NH_2 MNPs at different pH values can be seen in Table 1.

The extent of DNA adsorption on the FITC conjugated MNPs at different pH values was also evaluated. Similar approaches can be attributed to the FITC-conjugated silica coated iron oxide magnetic nanoparticles, *i.e.* Fe_3O_4@SiO_2@FITC MNPs, which can exhibit either a net positive or negative charge depending on the pH of the dispersion medium as illustrated in Scheme S2. Due to the cationic form of the FITC moiety and thiourea group originating from the primary amine ($-NH_2$) of APTES and the isothiocyanate group, it can be seen that at an acidic pH, a higher amount of DNA adsorption occurs for the FITC conjugated MNPs compared to the amine functionalized nanoparticles as shown in Fig. S5. Approximately 91% of the DNA added was adsorbed at pH 4.44, decreasing with increasing pH until dropping to a minimum value of approximately 61% at pH 11.01 regardless of temperature. The low adsorption of DNA seen at a pH of 11.01 is attributed to the formation of a di-anionic form of the FITC moiety, the primary group responsible for attracting DNA the particle surface through electrostatic interactions. However, there may always be a better interaction between DNA and FITC-conjugated particles because of the presence of the thiourea group. The total DNA adsorbed (Q) was calculated using the mass balance equation:

$$Q = \frac{(C_0 - C_f) \times V}{m} \quad (1)$$

where, Q is the adsorption level (μg mg^{-1}), C_0 is the initial DNA concentration (μg mL^{-1}), C_f is the final DNA concentration (μg mL^{-1}), V is the volume of DNA solution (mL) and m is the mass of adsorbent (mg).

Fig. 5b shows the results of the desorption percentages of DNA at various pH values, conducted at 40 °C and at a 5 mM ionic strength of the PBS buffer. As anticipated, it was discovered that pH had a significant impact on DNA desorption; when the pH changes from acidic to basic, desorption increases. This behavior can be explained by the reduction of the positively charged amino groups ($-NH_3^+$) on the surface of the magnetic nanoparticles because of the deprotonation of the amine functionalized silica coated iron oxide magnetic nanoparticles at basic pH. The results show that the highest DNA desorption efficiency (approximately 91% of the adsorbed DNA) was seen at pH 11.01, whereas pH 4.44 had a low DNA desorption efficiency (approximately 51% of the adsorbed DNA). On the other hand, the FITC on the magnetic nanoparticles may undergo a chemical change under alkaline conditions as its carboxylic groups become deprotonated, leading to lower desorption efficiencies. The highest DNA desorption efficiency (approximately 76% of the adsorbed DNA) was seen at pH 11.01. The experimental values of the DNA desorption efficiency of Fe_3O_4@SiO_2-NH_2 MNPs and Fe_3O_4@SiO_2@FITC MNPs at different pH values are shown in Table 2.

2.3 DNA sensing and quantification by fluorescence study

2.3.1 Effect of adsorbed DNA. Since the Fe_3O_4@SiO_2@FITC MNPs contain a highly pH sensitive fluorescent dye, they can exhibit either a net positive or negative surface charge depending on the pH of the dispersion medium, meaning

Table 2 The experimental values of DNA desorption efficiency (%) of amine functionalized silica coated iron oxide magnetic nanoparticles, *i.e.* Fe_3O_4@SiO_2-NH_2 MNPs, and FITC conjugated iron oxide magnetic nanoparticles, *i.e.* Fe_3O_4@SiO_2@FITC MNPs, at different pH values

pH	DNA desorption efficiency of Fe_3O_4@SiO_2-NH_2 MNPs (%)	DNA desorption efficiency of Fe_3O_4@SiO_2@FITC MNPs (%)
4.44	51.75 ± 4.36	50.10 ± 2.02
6.43	78.76 ± 2.16	52.88 ± 2.84
7.40	86.93 ± 3.15	64.65 ± 3.94
9.43	90.33 ± 4.02	70.79 ± 1.73
11.01	91.05 ± 3.05	76.85 ± 3.56

fluorescent labeled MNPs can serve as excellent probes for investigating DNA adsorption. This study aimed to observe the fluorescence quenching effect due to the adsorption of DNA influenced by the pH of the medium. As Fig. 6 shows, the absorption intensity at $\lambda_{(max)} = 494$ nm is significantly reduced at each pH when DNA ($\lambda_{(max)} = 260$ nm) is adsorbed by the Fe_3O_4@SiO_2@FITC nanoparticles, dropping to the lowest intensity at pH 4.44 regardless of temperature. The high adsorption of DNA seen at a pH of 4.44 results from the protonation of the FITC moiety, which is responsible for fluorescence quenching in addition to the effect of pH on absorption intensity. It can be said that the adsorption of DNA regulated by pH is secondarily responsible for fluorescence quenching regardless of the pH of the medium. Beside this, a Stern–Volmer analysis was conducted to investigate the fluorescence quenching mechanism of Fe_3O_4@SiO_2@FITC MNPs upon interaction with DNA, by systematically varying the

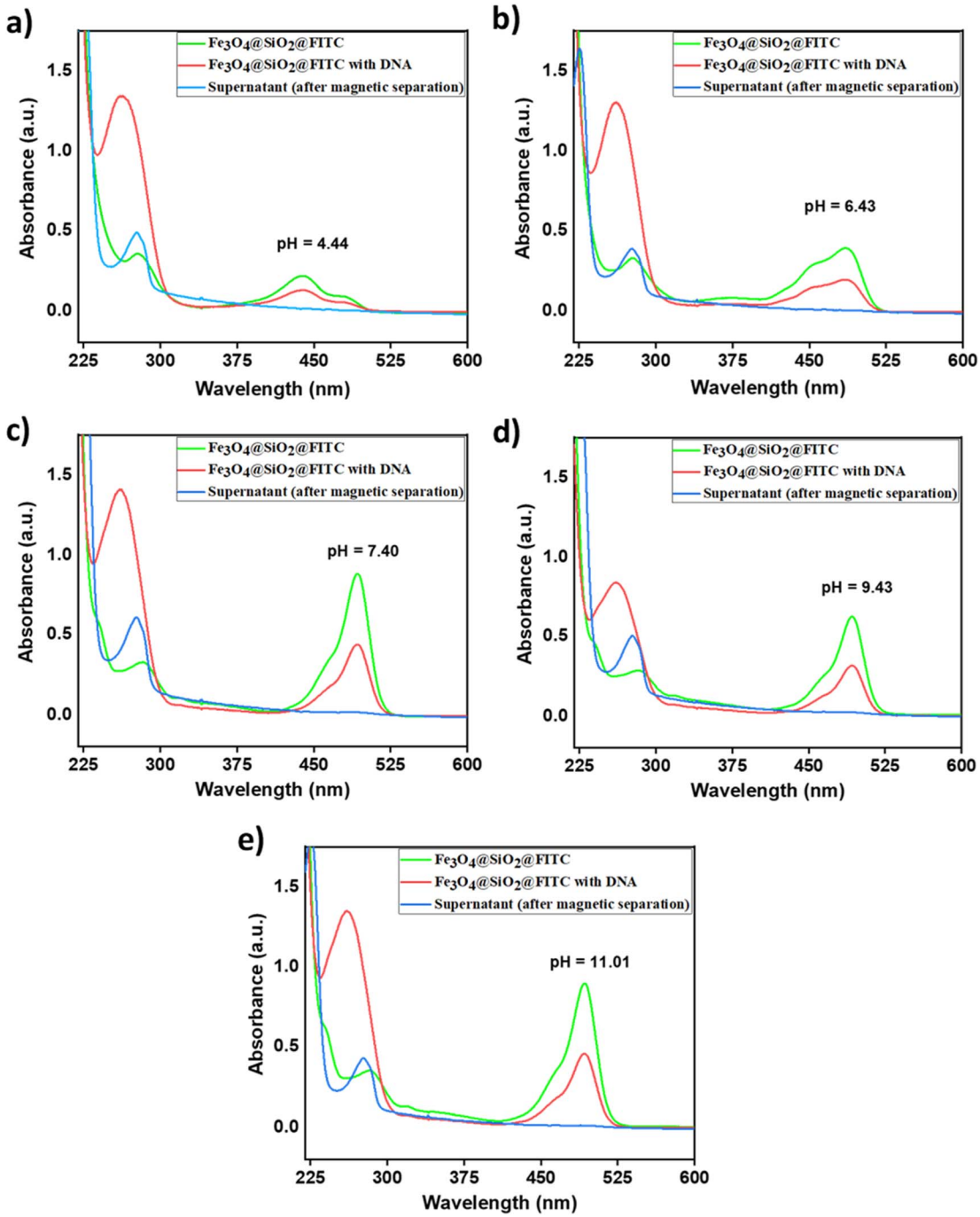

Fig. 6 (a–e) UV-Vis absorption spectra of FITC-conjugated iron oxide magnetic nanoparticles *i.e.*, Fe_3O_4@SiO_2@FITC MNPs before DNA adsorption (green curve), after DNA adsorption (red curve) and supernatant after magnetic separation (blue curve) at different pH values.

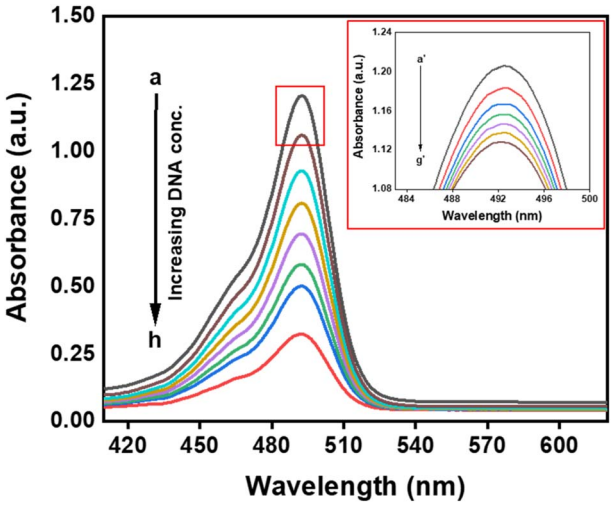

Fig. 7 UV-Vis absorption spectra of FITC-conjugated iron oxide magnetic nanoparticles, *i.e.* Fe_3O_4@SiO_2@FITC MNPs, after DNA adsorption at different DNA concentrations (a = 0.0 μg mL^{-1}, b = 5.0 μg mL^{-1}, c = 6.0 μg mL^{-1}, d = 7.0 μg mL^{-1}, e = 8.0 μg mL^{-1}, f = 9.0 μg mL^{-1}, g = 10.0 μg mL^{-1}, h = 11.0 μg mL^{-1}) at pH 7.40. Inset shows the absorption spectra at lower DNA concentrations (a' = 0.0 μg mL^{-1} to g' = 5.0 μg mL^{-1}) for observing minimum detection limit (MDL).

concentration of the quencher (DNA), as discussed in a later section.

However, as the pH of the medium decreases, the absorption intensity of the fluorescent nanoparticles decreases by more than 50% with the addition of DNA molecules as seen in the red curves of Fig. 6(a–e), suggesting rapid DNA adsorption. The secondary quenching effect may be due to formation of a DNA adsorption layer around the nanoparticles, blocking electronic transitions by potentially disrupting the electronic interactions responsible for strong light absorption.[47,48] For example, the electron transfer between the fluorophore and DNA bases such as guanine, which have a low ionization potential, reduces the excited-state energy of the fluorophore, leading to the quenching of both the absorbance and fluorescence intensities.[49–51] However, lower absorbance is observed due to the formation of the stable anionic and di-anionic form of the FITC moiety as illustrated in Scheme S2 and the lower DNA adsorption by the fluorescent nanoparticles at higher pH as shown in Fig. 5a.

2.3.2 Effect of DNA concentration. The UV-Vis absorption spectra of Fe_3O_4@SiO_2@FITC MNPs were recorded after DNA adsorption at different DNA concentrations ranging from 0.0 to 11.0 μg mL^{-1} at a pH of 7.40 as shown in Fig. 7. The Fe_3O_4@SiO_2@FITC MNPs show a characteristic absorption peak at $\lambda_{(max)}$ = 494 nm due to the fluorescein isothiocyanate (FITC) fluorophore. As DNA concentration increases, a progressive decrease in absorbance intensity is observed due to fluorescence quenching.

The inset graph in this figure focuses on lower DNA concentrations (0.0 to 5.0 μg mL^{-1}) to determine the smallest concentration at which a detectable change in absorbance occurs. The minimum detection limit (MDL) is identified as the lowest DNA concentration where a significant absorbance compared to the baseline of 0.0 μg mL^{-1} is observed. For example, if a noticeable absorbance decrease begins at 1.0 μg mL^{-1} or 2.0 μg mL^{-1}, then this concentration would be considered the MDL. The detection limit can be quantitatively estimated using the signal-to-noise ratio (S/N ≥ 3 rule), where the absorbance change should be at least three times the standard deviation of the baseline signal.

The adsorption isotherm depicted in Fig. 8a of Salmon sperm DNA on FITC-conjugated iron oxide magnetic nanoparticles was conducted in 5 mM PBS buffer at pH 7.40. The shape of the adsorption isotherm curve is comparable to a typical Langmuir curve, illustrating that the amount of adsorbed DNA increases with increasing DNA concentration. As the adsorption isotherm curves show, 11.0 μg mL^{-1} equilibrium DNA concentration in the feed yields the maximum adsorption. The amount was found to be 33.87 μg per mg of magnetic

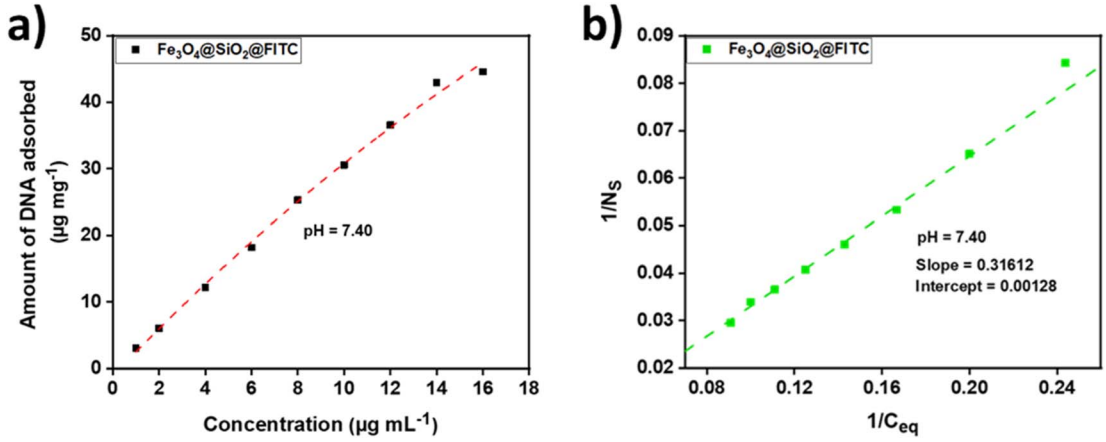

Fig. 8 (a) Adsorption isotherm at different DNA concentration at pH 7.40 (5 mM ionic strength of phosphate buffer solution, 25 °C temperature and 30 min incubation time). (b) Linear regression of $1/N_S$ (mg μg^{-1}) *versus* $1/C_{eq}$ (mL μg^{-1}) determined at pH 7.40 of the adsorption medium for adsorption isotherm at different DNA concentration (5 mM ionic strength of phosphate buffer solution, 25 °C temperature and 30 min incubation time).

particles at pH 7.40. Based on this result, it is assumed that a minimum of 47.0 μg mL^{-1} equilibrium concentration of DNA (derived from extrapolation of the adsorption isotherm model) is sufficient to achieve surface saturation of the magnetic particles with DNA at a given condition. Moreover, the large polyanionic DNA macromolecules potentially have less access to the particle surface due to their self-steric hindrance and electrostatic repulsion at higher DNA feed concentrations. Because of the good linear fit, the Langmuir model can be used to interpret the adsorption isotherm of DNA on the fluorescence magnetic nanoparticles indicating a monolayer adsorption, where DNA molecules interact with specific binding sites on the nanoparticle surface. The interaction involves electrostatic attractions, hydrogen bonding, or π–π stacking. The adsorption is reversible, meaning DNA can both adsorb and desorb from the surface as described by the equilibrium between these two processes. The Langmuir equation[52] can be written as follows:

$$\frac{1}{N_S} = \frac{1}{KN_S\infty}\frac{1}{C_{eq}} + \frac{1}{N_S\infty} \quad (2)$$

where N_S is the amount of DNA adsorbed (μg mg^{-1}), C_{eq} is the equilibrium concentration (μg mL^{-1}) of DNA in the PBS buffer, $N_S\infty$ is maximum amount of DNA adsorbed and K is the equilibrium constant of this adsorption and desorption process. K is defined as the affinity constant and equal to the ratio of adsorption (k_a) and desorption constant (k_d) *i.e.* $K = k_a/k_d$. Fig. 8b shows the linear regression of $1/N_S$ *versus* $1/C_{eq}$ determined at pH 7.40 in the adsorption medium. The experimental results are well fitted with the Langmuir model described in eqn (2). From the slope and intercept of the linear regression, we determined the affinity constant, $K = 0.04$, and the adsorption maximum, $N_S\infty = 78.1$ μg mg^{-1}, indicating that at saturation, each mg of nanoparticle can adsorb up to 78.1 μg of DNA. The low affinity constant suggests weak binding between DNA and the nanoparticle surface, implying that DNA molecules can readily desorb.

2.4 Fluorescence (FL) emission spectra analysis

Fluorescence emission spectra of FITC-conjugated iron oxide magnetic nanoparticles (Fe_3O_4@SiO_2@FITC MNPs) at varying particle concentrations, prior to DNA adsorption, were recorded in phosphate buffer (pH 7.40, 5 mM ionic strength) at 25 °C (Fig. 9a). All spectra displayed a dominant emission peak centered at ~521 nm, characteristic of FITC upon excitation at 494 nm. An additional peak centered at ~497 nm was observed for nanoparticles in aqueous medium, arising from fluorescein emission when conjugated to Fe_3O_4, consistent with the coexistence of different fluorescein ionic forms and excited-state proton transfer processes reported in the literature.[53,54] Increasing nanoparticle concentration led to a progressive enhancement of fluorescence intensity, attributable to the greater number of FITC moieties within the optical path. The near-linear trend at lower concentrations suggests minimal reabsorption or concentration quenching. At higher concentrations, intensity enhancement plateaued, with a slight decrease at 497 nm, likely due to inner filter effects and/or self-quenching *via* non-radiative energy transfer between closely spaced fluorophores.[55,56] These results indicate that the fluorescence output of the Fe_3O_4@SiO_2@FITC MNPs system can be tuned by nanoparticle concentration, although excessive loading should be avoided to minimize quenching.

The fluorescence emission spectra of FITC-conjugated iron oxide magnetic nanoparticles upon exposure to increasing concentrations of DNA at physiological pH (7.40) in phosphate buffer (5 mM) at 25 °C was illustrated in Fig. 9b. Following DNA adsorption, Fe_3O_4@SiO_2@FITC MNPs retained a stable fluorescence excitation maximum at 494 nm, with an emission band centered at ~521 nm. The spectral profile remained similar to that of the Fe_3O_4@SiO_2@FITC MNPs; however, a notable increase in fluorescence intensity was observed. This enhancement is attributed to interactions between DNA and the FITC moieties, which may restrict fluorophore mobility, reduce

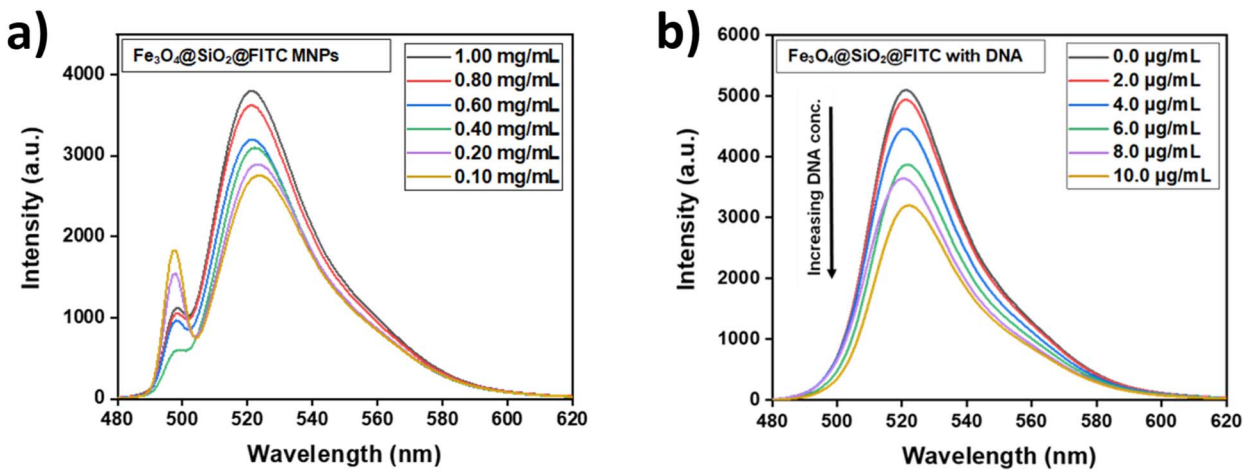

Fig. 9 (a) Fluorescence emission spectra of FITC-conjugated iron oxide magnetic nanoparticles (Fe_3O_4@SiO_2@FITC MNPs) at varying particle concentrations (0.01 to 1.00 mg mL^{-1}) prior to DNA adsorption. (b) Fluorescence emission spectra of FITC-conjugated iron oxide magnetic nanoparticles (Fe_3O_4@SiO_2@FITC MNPs) after DNA adsorption at different DNA concentrations (0.0 to 10.0 μg mL^{-1}) recorded at pH 7.40 in phosphate buffer (5 mM ionic strength, 25 °C; excitation at 494 nm).

non-radiative relaxation pathways, or alter the local microenvironment to favor radiative decay.[57] Notably, the secondary emission peak at ~497 nm, present in the Fe_3O_4@SiO_2@FITC MNPs was markedly diminished upon DNA binding, likely due to changes in the relative population of fluorescein ionic species induced by electrostatic and hydrogen-bonding interactions with DNA.[58] The pristine Fe_3O_4@SiO_2@FITC MNPs (0.0 μg mL^{-1} DNA) exhibit a strong fluorescence emission peak characteristic of FITC. As the DNA concentration increases, a progressive decrease in fluorescence intensity is observed, indicating quenching of the FITC fluorescence. This quenching effect suggests effective adsorption or interaction of DNA molecules onto the nanoparticle surface, which likely leads to changes in the local environment around FITC and possibly energy or electron transfer processes causing fluorescence suppression.[59,60] The trend of fluorescence intensity reduction with increasing DNA concentration confirms the sensitivity of Fe_3O_4@SiO_2@FITC MNPs towards DNA binding, making them suitable for biosensing applications.

2.5 Elucidation of fluorescence quenching mechanism by Stern–Volmer Analysis

To investigate the fluorescence quenching mechanism of the Fe_3O_4@SiO_2@FITC MNPs with DNA, a Stern–Volmer analysis was performed by systematically varying the concentration of the quencher, in this case, low molecular weight salmon sperm DNA (MW = 100 kDa). The fluorescence intensity of the FITC-conjugated nanoparticles was recorded at a fixed excitation wavelength (494 nm) while increasing the DNA concentration in the solution. The Stern–Volmer equation[61] was used to analyze the quenching behavior.

$$\frac{F_0}{F} = 1 + K_{SV}[\mathrm{DNA}] \quad (3)$$

where, F_0 is the fluorescence intensity in the absence of quencher at maximum emission wavelength 521 nm, F is the fluorescence intensity in the presence of quencher, K_{SV} is the Stern–Volmer quenching constant, and [DNA] is the concentration of DNA.

The Stern–Volmer plot of F_0/F *versus* [DNA] was obtained (Fig. 10a), showing a linear relationship at lower DNA concentrations, which suggests a predominantly dynamic quenching mechanism due to collisional interactions between the FITC fluorophore and DNA molecules. However, at higher DNA concentrations, the plot deviated from linearity, indicating a mixed quenching process involving both dynamic and static quenching mechanisms. The static quenching likely arises from the formation of non-fluorescent complexes between DNA and FITC on the nanoparticle surface. These observations imply that DNA binding alters the local environment of the FITC fluorophore, reducing fluorescence *via* both transient collisions and stable complex formation.[62,63] The high Stern–Volmer quenching constant (K_{SV}) value reflects effective interaction between DNA molecules and FITC fluorophores on the nanoparticle surface, likely facilitated by electrostatic attraction and close-range energy or electron transfer pathways. The quenching behavior confirms the effective interaction of the biosensor with DNA, validating its potential for sensitive fluorescence-based DNA detection. From the calibration curve obtained in Fig. 10b, the limit of detection (LOD) for DNA was estimated using the 3σ/|slope| criterion, yielding a value of 0.0785 μg mL^{-1} (where standard deviation, σ = 5.729). This sensitivity aligns well with the observed data in the UV-Vis absorption spectra (Fig. 7), where measurable signal changes were evident even at low DNA concentrations, confirming the suitability of the developed nanoparticle-based system for trace-level DNA detection. The fluorescent on-off switching mechanism of Fe_3O_4@SiO_2@FITC MNPs with bound and unbound DNA is illustrated in Scheme 3.

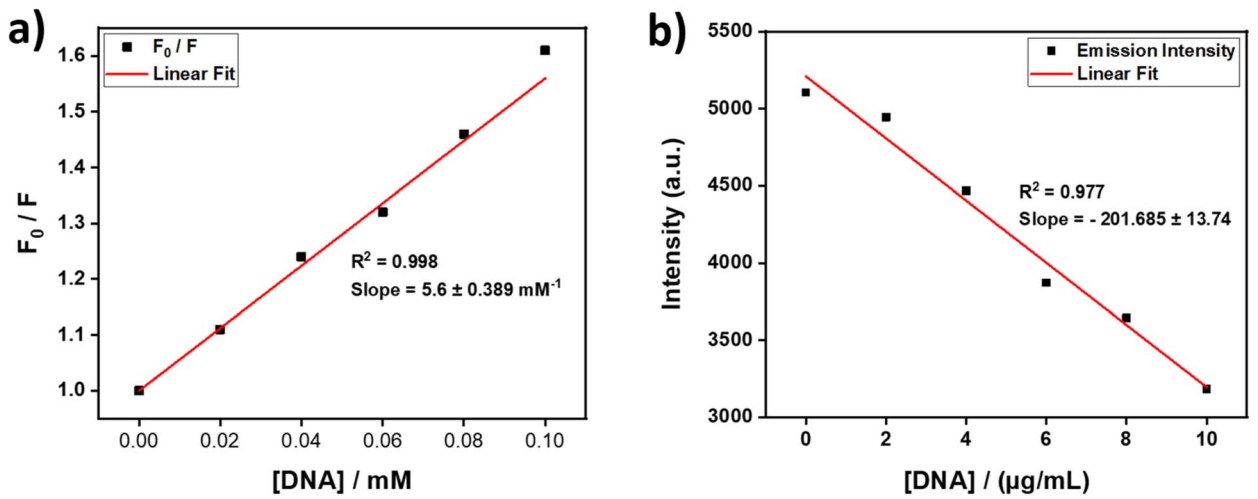

Fig. 10 (a) Stern–Volmer plots of F_0/F *versus* [DNA]/mM for fluorescence quenching of Fe_3O_4@SiO_2@FITC MNPs by salmon sperm DNA. The linear fit yielded a Stern–Volmer quenching constant (K_{SV}) from the slope of 5.6 ± 0.389 mM^{-1} with a high coefficient of determination (R^2 = 0.998), indicating strong and consistent quenching efficiency. (b) Fluorescence emission intensity *versus* DNA concentration (μg mL^{-1}) for the calculation of limit of detection (LOD). The linear fit yielded a |slope| = 201.685 ± 13.74 with a high coefficient of determination (R^2 = 0.977). The limit of detection for DNA was found to be 0.0785 μg mL^{-1}.

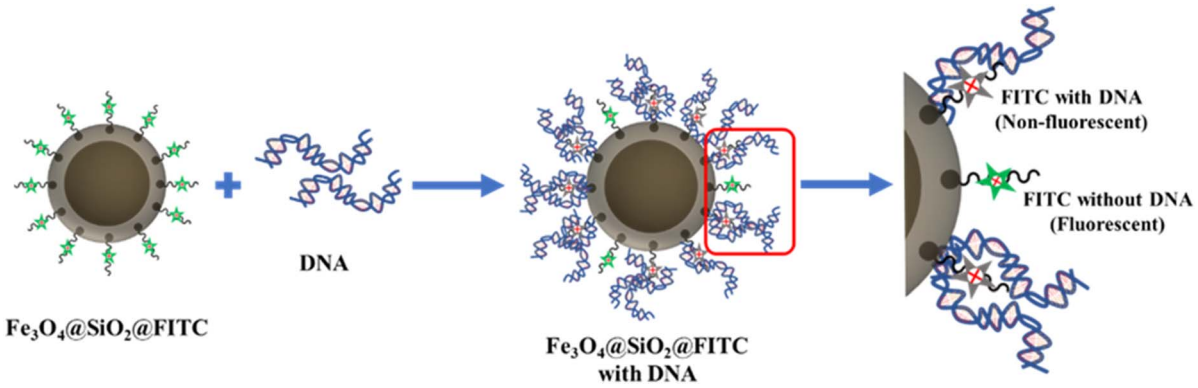

Scheme 3 Schematic representation of fluorescence on-off switching mechanism of FITC-conjugated iron oxide magnetic nanoparticles *i.e.*, Fe_3O_4@SiO_2@FITC MNPs with bound and unbound DNA.

2.6 Agarose gel electrophoresis

All samples yielded distinct, low molecular weight DNA bands upon agarose gel electrophoresis (showed in Fig. 11), demonstrating effective isolation. The DNA ladder in the rightmost lane provided clear resolution of low base pair markers, confirming accurate size estimation.

The predominant bands across sample lanes migrated consistently with DNA fragments in the low hundreds of base pairs, reflecting a largely uniform fragment population with minimal fragmentation. Minor smearing observed in some lanes indicates a small proportion of shorter fragments or slight degradation; however, the overall electrophoretic profile confirms that the isolated DNA maintains structural integrity with low fragmentation, making it suitable for subsequent analyses.

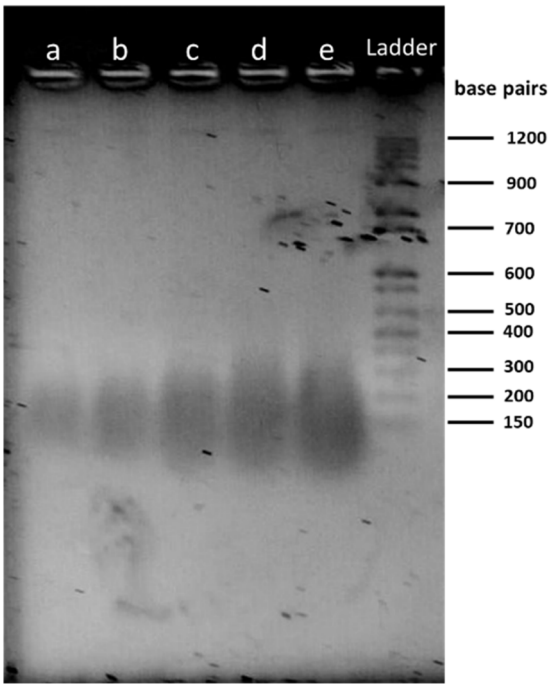

Fig. 11 Agarose gel electrophoresis analysis of low molecular weight salmon sperm DNA, magnetically separated by FITC-conjugated iron oxide magnetic nanoparticles (Fe_3O_4@SiO_2@FITC MNPs) and subsequent redispersion in PBS buffer (pH 7.40). Sample wells contain DNA at the concentrations of $a = 0.5$ μg mL^{-1}, $b = 1.0$ μg mL^{-1}, $c = 2.0$ μg mL^{-1}, $d = 3.0$ μg mL^{-1} and $e = 4.0$ μg mL^{-1}. The rightmost lane shows a molecular weight (base pair) DNA ladder for size reference.

3 Experimental

3.1 Materials

Commercially available chemicals were utilized in the synthesis of the oleic acid coated iron oxide magnetic nanoparticles, *i.e.* Fe_3O_4@OA MNPs; the silica coted iron oxide magnetic nanoparticles, *i.e.* Fe_3O_4@SiO_2 MNPs; the amine functionalized silica coated iron oxide magnetic nanoparticles, *i.e.* Fe_3O_4@SiO_2-NH_2 MNPs; and the FITC labeled silica coated iron oxide magnetic nanoparticles, *i.e.* Fe_3O_4@SiO_2@FITC MNPs. All chemicals, including the precursors: anhydrous Iron(III) chloride ($FeCl_3$, 99.99%) and iron(II) chloride tetrahydrate ($FeCl_2 \cdot 4H_2O$) purchased from Sisco Research Laboratories (SRL), India; the surfactants: oleic acid (OA, 90%), Igepal®CO-520 (90%), and tetraethyl orthosilicate (TEOS, 98%) purchased from Sigma-Aldrich, USA; the coupling agent: 3-aminopropyltriethoxysilane (APTES, 90%) purchased from TCI, Japan; and fluorescein isothiocyanate (FITC) and Salmon sperm DNA also purchased from Sigma-Aldrich, USA, were stored in the refrigerator in the lab before being used. Ethanol was distilled before use, and the *n*-hexane, NaOH and ammonium hydroxide (25%) solutions were analytical grade and used without further purification. In addition, distilled deionized water was used throughout the study.

3.2 Methods

3.2.1 Synthesis of Fe_3O_4@OA magnetic nanoparticles. Oleic acid coated iron oxide magnetic nanoparticles, *i.e.* Fe_3O_4@OA MNPs, were synthesized using a coprecipitation method,[41] with a little modification using anhydrous iron(III) chloride ($FeCl_3$) and iron(II) chloride tetrahydrate ($FeCl_2 \cdot 4H_2O$) salts at a Fe^{3+}/Fe^{2+} molar ratio of 2 : 1. The entire synthesis was conducted under an oxygen-free condition by ensuring the continuous flow of nitrogen gas. Briefly, the reaction equipment

was set up as prescribed, and 5.76 g of NaOH were dissolved in 100.0 mL of deionized (DI) water. The solution was then transferred to a 250 mL three-neck round bottom flask, and the temperature was raised to 90 °C with continuous stirring using a mechanical stirrer at 400 rpm. Subsequently, 2.61 g of anhydrous $FeCl_3$ and 1.35 g of $FeCl_2 \cdot 4H_2O$ were dissolved in 50.0 mL of DI water under purging nitrogen gas and added dropwise to the reaction from a burette for 60 min. The color of the solution immediately turned dark black, and the pH of the solution was maintained at approximately 10 to 11 throughout the reaction. After 30 min of reaction, 2.0 mL of oleic acid were added, and the reaction mixture was stirred for additional 1 h at the same temperature. Finally, the solution was cooled to room temperature and washed with DI water and ethanol 5 times using magnetic separation. After washing, oleic acid coated iron oxide magnetic nanoparticles, *i.e.* Fe_3O_4@OA MNPs, were dispersed in cyclohexane for storage. All the samples were dried before conducting structure, particle size and magnetic characterization.

3.2.2 Synthesis of Fe_3O_4@SiO_2 magnetic nanoparticles. Silica coated iron oxide magnetic nanoparticles, *i.e.* Fe_3O_4@SiO_2 MNPs, were prepared according to the procedure reported in the literature.[64] A reverse microemulsion (water-in-oil; w/o) method was followed for preparing the silica coted iron oxide magnetic nanoparticles, *i.e.* Fe_3O_4@SiO_2 MNPs. Briefly, 3.52 g of Igepal®CO-520 were dispersed in 41.0 mL of cyclohexane in a 250 mL conical flask and ultrasonicated for 10 minutes. Then, 10.0 mg of oleic acid coated iron oxide magnetic nanoparticles, *i.e.* Fe_3O_4@OA MNPs, were dispersed ultrasonically in 4.0 mL of cyclohexane for 20 minutes. Next the MNP suspension was added dropwise to the surfactant solution, followed by sonication and shaking for 30 minutes. Subsequently, 550 μL of ammonium hydroxide (25%) solution were added to this mixture, followed by 300 μL of tetraethyl orthosilicate (TEOS). Finally, the mixture was gently shaken for 48 hours at room temperature to introduce the silica layer onto the surface of Fe_3O_4 nanoparticles. The resulting Fe_3O_4@SiO_2 MNPs were then thoroughly washed five times with an ethanol–water mixture, collected through magnetic decantation to remove the surfactants and then dispersed in ethanol for storage.

3.2.3 Surface modification of Fe_3O_4@SiO_2 nanoparticles. The surface modification of Fe_3O_4@SiO_2 MNPs was conducted using amino-silane (APTES, 3-aminopropyltriethoxysilane) in an ethanol–water mixture. For this purpose, 41.0 mg of Fe_3O_4@SiO_2 magnetic nanoparticles were dispersed in 25.0 mL of ethanol–water mixture by applying ultrasonication for 2 h. Subsequently, 100 μl of ammonium hydroxide (25%) and 100 μl of amino-silane coupling agent (APTES) were added dropwise into the dispersion. The solution was then heated to reflux for 4 h (*e.g.*, 80 to 90 °C) and stirred at 300 rpm for an additional 24 h at room temperature. Finally, the nanoparticles obtained, *i.e.* Fe_3O_4@SiO_2-NH_2 MNPs, were separated magnetically; the residual amino-silanes were removed by rinsing the sample in ethanol three times with 30 seconds of ultrasonication and the MNPs were re-dispersed in ethanol.

3.2.4 Fluorescein coupling with Fe_3O_4@SiO_2-NH_2 nanoparticles. For this procedure, 1.0 mg of fluorescein isothiocyanate (FITC) was dissolved in 10.0 mL of absolute ethanol. Then, 200 μl of ammonium hydroxide were added. Subsequently, 10.0 mg of amine functionalized silica coated iron oxide magnetic nanoparticles, *i.e.* Fe_3O_4@SiO_2-NH_2 MNPs, were added to the solution. The reactants were stirred for 16 h at room temperature in a dark environment and solid products were recovered through magnetic separation. The nanoparticles obtained, FITC labeled silica coated iron oxide magnetic nanoparticles, *i.e.* Fe_3O_4@SiO_2@FITC MNPs, were rinsed three times with ethanol and twice with DI water to remove the physically adsorbed FITC molecules. Three minutes of sonication were applied to each cycle.

3.3 Characterizations

The structural functionality of the particles formed at different stages was analyzed using an FTIR Spectrophotometer (PerkinElmer, FTIR-100, USA) across the 4000–200 cm^{-1} range. The magnetic characteristics were investigated using a DXV-9000 series vibrating sample magnetometer manufactured by Xiamen Dexing Magnet Tech. Co., Ltd, China. At 300.0 K, the magnetic property of the dry powder particles was determined, with $H = 1318$ Oe and $m = 0.3326$ emu. The XRD patterns were obtained by using a Rigaku (Tokyo, Japan) Ultima IV RINT D/max-kA diffractometer with Cu K_α radiation ($\lambda = 1.54178$ Å) under standard room conditions. TEM micrographs were obtained at an accelerating voltage of 120 kV and a beam current of 8 μA using a Hitachi 7839 (USA) instrument with different magnifications. The surface nature and elemental study were conducted using a scanning electron microscope (SEM) with a ZEOL, JSM-IT800 SEM system applying a landing voltage ranging from 1.00 kV to 30.00 kV and magnifications ranging from 5× to 30 000×. UV-Vis absorption spectra of fluorescent magnetic nanoparticles were recorded using a UV-1240 (Shimadzu Corporation, Japan), while fluorescence emission spectra of the synthesized nanoparticles and the interaction of fluorophore with DNA was conducted using a fluorescence spectrophotometer F-7000 (Hitachi High-Tech Corporation, Japan), using an excitation wavelength of 494 nm. Quartz cuvettes (1 cm path length) were used for all optical measurements. Gel electrophoresis analysis was performed using vertical gel electrophoresis system CVS10CBS (Cleaver, UK).

3.4 Data analysis

All experiments were performed in triplicate ($n = 3$) unless otherwise specified. The obtained data are presented as the mean value ± standard deviation (SD). Statistical analysis was carried out using OriginPro 2019b and graphical data were plotted accordingly. Where relevant, statistical significance was assessed using Student's *t*-test with $p < 0.05$ considered statistically significant.

3.5 DNA adsorption procedure

For the DNA adsorption study with chemically functionalized MNPs at different pH values, 1.0 mg of amine functionalized silica coated iron oxide magnetic nanoparticles, *i.e.* Fe_3O_4@SiO_2-NH_2 MNPs, and 1.0 mg of fluorescent iron oxide magnetic

nanoparticles, *i.e.* Fe_3O_4@SiO_2@FITC MNPs, were added separately to vials containing a 5.0 mL phosphate buffer solution (5 mM PBS) at five pH values, specifically, 4.44, 6.43, 7.40, 9.43, and11.01. After ultrasonication for 30 s, 50.0 μg of salmon sperm DNA were added to the dispersions, which were then incubated for 30 min at laboratory temperature (25 °C) accompanied by stirring at 1000 rpm. Finally, the magnetic latex particles with the adsorbed DNA were separated as quickly as possible using an external magnet and centrifugation at 10 000 rpm for 5 min, with the resulting clear supernatant then being collected. The concentration of nucleic acids in the supernatant can be readily calculated by measuring the absorbance at 260 nm in a UV-Vis spectrophotometer using a standard calibration curve (plotting DNA concentration against absorbance at different pH values). The amount of DNA adsorbed by the magnetic nanoparticles (μg DNA per mg dry particles) was calculated from both the initial and final DNA concentrations in the clear supernatant.

3.6 DNA desorption procedure

For the DNA Desorption procedure, 5.0 mL of desorption buffer (PBS) was added to the vial containing the DNA-adsorbed magnetic latex particles. The particles were thoroughly dispersed, and the vial was then placed in a temperature-controlled oil-bath accompanied by stirring at 1000 rpm at a temperature of 40 °C for 45 min. After incubation, magnetic separation using an external magnet and centrifugation at 10 000 rpm for 5 min, the clear supernatant was collected for absorbance measurement at 260 nm. Using a standard calibration curve (plotting DNA concentration against absorbance at different pH values), the percentage of DNA desorption was determined based on the desorbed DNA amount and the initial DNA adsorbed on the magnetic latex particles. A schematic representation of the entire DNA adsorption and desorption process of magnetic particles is illustrated in Scheme 4.

3.7 Sample preparation for UV-vis absorption study

For the absorption study at pH 7.40, 1.0 mg of FITC-conjugated Fe_3O_4@SiO_2@FITC MNPs was added to vials, each containing a 5.0 mL phosphate buffer solution (5 mM PBS). After ultrasonication for 30 s, different amounts (25, 30, 35, 40, 45, 50, 55 μg) of Salmon sperm DNA were added to the dispersions, which were then incubated for 30 min at 25 °C accompanied by stirring at 1000 rpm. Finally, the MNPs with adsorbed DNA were separated as quickly as possible using an external magnet and centrifugation at 10 000 rpm for 5 min, and the clear supernatant was collected. The concentration of DNA in the supernatant can readily be calculated by measuring the absorbance at 260 nm in a UV-Vis spectrophotometer using a standard calibration curve (plotting DNA concentration against absorbance at different pH values). The amount of DNA adsorbed (μg DNA per mg dry particles) was calculated from both the initial and the final DNA concentrations in the clear supernatant. A new approach for adsorbed DNA sensing and quantification was derived by taking continuous absorption spectra and measuring the absorbance at 494 nm for the pH conditions of 4.44, 6.43, 7.40, 9.43, 11.01 in the UV-Vis spectrophotometer.

3.8 Sample preparation for fluorescence emission study

A stock suspension of FITC-conjugated iron oxide magnetic nanoparticles (Fe_3O_4@SiO_2@FITC MNPs, 5.0 mg) was prepared in phosphate-buffered saline (PBS, pH 7.40, 5 mM ionic strength) to a final volume of 5.0 mL, followed by sonication for 10 min to ensure uniform dispersion. The suspension was serially diluted to obtain nanoparticle concentrations of 0.10, 0.20, 0.40, 0.60, 0.80, and 1.00 mg mL^{-1}. A blank solution containing only PBS was used for baseline correction. Fluorescence emission spectra of the Fe_3O_4@SiO_2@FITC MNPs at different particle concentrations, prior to DNA adsorption, were then recorded. For the Stern–Volmer analysis, FITC-conjugated iron oxide magnetic nanoparticles (Fe_3O_4@SiO_2@FITC MNPs) were dispersed in phosphate-buffered saline (PBS, pH 7.40, 5 mM ionic strength) to a concentration of 1.0 mg mL^{-1} by sonication for 10 min. Equal volumes of this nanoparticle suspension were mixed with DNA solutions of varying concentrations to obtain final DNA concentrations of 0.00, 0.02, 0.04, 0.06, 0.08, and 0.10 mM. The mixtures were incubated at room temperature for 30 min to allow interaction between DNA and the nanoparticles. Steady-state fluorescence emission spectra were recorded using a fluorescence spectrophotometer with an excitation wavelength of 494 nm and the fluorescence intensity at the emission maximum (521 nm) was measured for each DNA concentration for Stern–Volmer analysis.

3.9 Agarose gel electrophoresis

Low molecular weight salmon sperm DNA was magnetically separated using FITC-conjugated iron oxide magnetic nanoparticles (Fe_3O_4@SiO_2@FITC MNPs) in PBS (pH 7.4) following

Scheme 4 Schematic illustration of the adsorption and desorption procedure of DNA using functionalized/modified iron oxide magnetic nanoparticles.

the previously described adsorption–desorption protocol. The MNPs were collected with a permanent magnet, washed three times with PBS, and redispersed. The final concentrations of the recovered DNA were adjusted to 0.5, 1.0, 2.0, 3.0, and 4.0 μg mL^{-1}, as determined by a NanoDrop spectrophotometer. Each sample were loaded into separate wells of a 2% agarose gel prepared in 1× TAE buffer. Electrophoresis was performed at 100 V for 40 min, and a 100 bp DNA ladder was included as a molecular size marker.

4 Conclusion

This study demonstrates the successful synthesis and characterization of multifunctional fluorescent iron oxide magnetic nanoparticles (*i.e.* Fe_3O_4@SiO_2@FITC MNPs) for dual applications in DNA separation and real-time visualization. We have demonstrated that separation and visual quantification of DNA using targeted fluorescent magnetic nanoparticles are possible even without separation of the DNA from the medium containing the biomolecules. The UV-Vis absorption and fluorescence emission intensity of the prepared nanoparticles dramatically decreasing through the adsorption of DNA molecules. Targeted DNA visualization, therefore, seems possible when using DNA solutions and is more effective than procedures requiring a separation technique. These findings highlight the promise of these nanoparticles as a versatile platform in molecular biology, paving the way for further advancements in disease diagnostic applications. Future research may focus on exploring their application in complex biological samples, functionalizing the nanoparticle surface for sequence-specific DNA detection, and integrating the system into point-of-care diagnostic devices. Such developments could expand their utility across diverse biomedical and analytical applications.

Author contributions

Md. Shamiull Alim Munna performed analytical assays and contributed to writing, editing and revising the manuscript. Md. Mazharul Islam contributed to manuscript writing and editing. Mohammad Ahasanur Rabbi carried out SEM and EDS analysis and data interpretation. O. Thompson Mefford and Alexander Malaj conducted TEM analysis, investigation, and validation, and contributed to the original draft. Md. Shahidul Islam contributed to funding acquisition, resources, and investigation. Hasan Ahmad was responsible for supervision, project administration, and manuscript review and editing. Md. Mahbubor Rahman contributed to conceptualization, study design, supervision, project administration, funding acquisition, and manuscript review and editing. All authors reviewed and approved the final manuscript.

Conflicts of interest

The authors declare that there are no financial interests or personal relationships that could have influenced the work presented in this article.

Data availability

Further data associated with this work are available from the corresponding author upon reasonable request.

All supporting data are available in the supplementary information (SI). Supplementary information is available. See DOI: https://doi.org/10.1039/d5ra04563k.

Acknowledgements

The authors gratefully acknowledge the Ministry of Science and Technology, Bangladesh, for financial support of this work. We also thank the Polymer Colloids and Nanomaterials (PCN) Research Lab and the researchers who assisted with chemical analyses for their valuable support.

References

1 J.-H. Kang, Y. T. Kim, K. Lee, H.-M. Kim, K. G. Lee, J. Ahn, J. Lee, S. J. Lee and K.-B. Kim, An Electrophoretic DNA Extraction Device Using a Nanofilter for Molecular Diagnosis of Pathogens, *Nanoscale*, 2020, **12**(8), 5048–5054, DOI: 10.1039/C9NR10675H.

2 G. He, Y. Chen, C. Zhu, J. Zhou, X. Xie, R. Fei, L. Wei, H. Zhao, H. Chen and H. Zhang, Application of Plasma Circulating Cell-Free DNA Detection to the Molecular Diagnosis of Hepatocellular Carcinoma, *Am. J. Transl. Res.*, 2019, **11**(3), 1428–1445.

3 D. C. Duffy, Digital Detection of Proteins, *Lab Chip*, 2023, **23**(5), 818–847, DOI: 10.1039/D2LC00783E.

4 S. Delshadi, M. Fratzl, O. Ramel, P. Bigotte, P. Kauffmann, D. Kirk, V. Masse, M. P. Brenier-Pinchart, H. Fricker-Hidalgo, H. Pelloux, F. Bruckert, C. Charrat, O. Cugat, N. M. Dempsey, T. Devillers, P. Halfon, A. Leroy, M. Weidenhaupt and P. N. Marche, Magnetically Localized and Wash-Free Fluorescence Immunoassay (MLFIA): Proof of Concept and Clinical Applications, *Lab Chip*, 2023, **23**(4), 645–658, DOI: 10.1039/D2LC00926A.

5 N. Miguel-Sancho, O. Bomatí-Miguel, G. Colom, J.-P. Salvador, M.-P. Marco and J. Santamaría, Development of Stable, Water-Dispersible, and Biofunctionalizable Superparamagnetic Iron Oxide Nanoparticles, *Chem. Mater.*, 2011, **23**(11), 2795–2802, DOI: 10.1021/cm1036452.

6 S. Laurent, D. Forge, M. Port, A. Roch, C. Robic, L. Vander Elst and R. N. Muller, Magnetic Iron Oxide Nanoparticles: Synthesis, Stabilization, Vectorization, Physicochemical Characterizations, and Biological Applications, *Chem. Rev.*, 2008, **108**(6), 2064–2110, DOI: 10.1021/cr068445e.

7 D. T. Nguyen and K. Kim, Analysis on Development of Magnetite Hollow Spheres through One-pot Solvothermal Process, *AIChE J.*, 2013, **59**(10), 3594–3600, DOI: 10.1002/aic.14139.

8 A. Heddini, C. J. Treutiger and M. Wahlgren, Enrichment of Immunoglobulin Binding Plasmodium Falciparum-Infected Erythrocytes Using Anti-Immunoglobulin-Coated Magnetic Beads, *Am. J. Trop. Med. Hyg.*, 1998, **59**(5), 663–666, DOI: 10.4269/ajtmh.1998.59.663.

9 I. M. Prados, A. Barrios-Gumiel, F. J. De La Mata, M. L. Marina and M. C. García, Magnetic Nanoparticles Coated with Carboxylate-Terminated Carbosilane Dendrons as a Reusable and Green Approach to Extract/Purify Proteins, *Anal. Bioanal. Chem.*, 2022, **414**(4), 1677–1689, DOI: 10.1007/s00216-021-03794-7.

10 U. Jeong, X. Teng, Y. Wang, H. Yang and Y. Xia, Superparamagnetic Colloids: Controlled Synthesis and Niche Applications, *Adv. Mater.*, 2007, **19**(1), 33–60, DOI: 10.1002/adma.200600674.

11 S. Y. Çelik, K. Solak and A. Mavi, Sulfanilamide Modified Magnetic Nanoparticles for Purification of Carbonic Anhydrase from Bovine Blood, *Appl. Biochem. Biotechnol.*, 2023, **195**(6), 3900–3913, DOI: 10.1007/s12010-022-03983-9.

12 M. Mostafaei, S. N. Hosseini, M. Khatami, A. Javidanbardan, A. A. Sepahy and E. Asadi, Isolation of Recombinant Hepatitis B Surface Antigen with Antibody-Conjugated Superparamagnetic Fe3O4/SiO2 Core-Shell Nanoparticles, *Protein Expression Purif.*, 2018, **145**, 1–6, DOI: 10.1016/j.pep.2017.12.004.

13 L. Griffiths and D. Chacon-Cortes, Methods for Extracting Genomic DNA from Whole Blood Samples: Current Perspectives, *J. Biorepos. Sci. Appl. Med.*, 2014, **1**, 1–9, DOI: 10.2147/BSAM.S46573.

14 A. Gautam, Phenol-Chloroform DNA Isolation Method, in *DNA and RNA Isolation Techniques for Non-Experts*, Techniques in Life Science and Biomedicine for the Non-Expert, Springer International Publishing, Cham, 2022, pp. 33–39, DOI: 10.1007/978-3-030-94230-4_3.

15 K. Budelier and J. Schorr, Purification of DNA by Anion-Exchange Chromatography, *Curr. Protoc. Mol. Biol.*, 1998, **42**(1), 11–18, DOI: 10.1002/0471142727.mb0201bs42.

16 A. Gautam, Isolation of DNA from Blood Samples by Salting Method, in *DNA and RNA Isolation Techniques for Non-Experts*, Techniques in Life Science and Biomedicine for the Non-Expert, Springer International Publishing, Cham, 2022, pp. 89–93, DOI: 10.1007/978-3-030-94230-4_12.

17 C.-L. Chiang and C.-S. Sung, Purification of Transfection-Grade Plasmid DNA from Bacterial Cells with Superparamagnetic Nanoparticles, *J. Magn. Magn. Mater.*, 2006, **302**(1), 7–13, DOI: 10.1016/j.jmmm.2005.08.022.

18 X. Guo, F. Hu, Z. Yong, S. Zhao, Y. Wan, B. Wang and N. Peng, Magnetic Nanoparticle-Based Microfluidic Platform for Automated Enrichment of High-Purity Extracellular Vesicles, *Anal. Chem.*, 2024, **96**(18), 7212–7219, DOI: 10.1021/acs.analchem.4c00795.

19 M. Dinc, C. Esen and B. Mizaikoff, Recent Advances on Core–Shell Magnetic Molecularly Imprinted Polymers for Biomacromolecules, *TrAC, Trends Anal. Chem.*, 2019, **114**, 202–217, DOI: 10.1016/j.trac.2019.03.008.

20 Y. Chen, Y. Liu, Y. Shi, J. Ping, J. Wu and H. Chen, Magnetic Particles for Integrated Nucleic Acid Purification, Amplification and Detection without Pipetting, *TrAC, Trends Anal. Chem.*, 2020, **127**, 115912, DOI: 10.1016/j.trac.2020.115912.

21 A. P. Tiwari, R. K. Satvekar, S. S. Rohiwal, V. A. Karande, A. V. Raut, P. G. Patil, P. B. Shete, S. J. Ghosh and S. H. Pawar, Magneto-Separation of Genomic Deoxyribose Nucleic Acid Using pH Responsive Fe_3O_4 @silica@chitosan Nanoparticles in Biological Samples, *RSC Adv.*, 2015, **5**(11), 8463–8470, DOI: 10.1039/C4RA15806G.

22 A. N. Danthanarayana, D. C. Manatunga, R. M. De Silva, N. V. Chandrasekharan and K. M. Nalin De Silva, Magnetofection and Isolation of DNA Using Polyethyleneimine Functionalized Magnetic Iron Oxide Nanoparticles, *R. Soc. Open Sci.*, 2018, **5**(12), 181369, DOI: 10.1098/rsos.181369.

23 J. Xu, D. Chen, Y. Yang, H. Gong, W. Gao and H. Xiao, A One Step Method for Isolation of Genomic DNA Using Multi-Amino Modified Magnetic Nanoparticles, *RSC Adv.*, 2021, **11**(6), 3324–3332, DOI: 10.1039/D0RA09409A.

24 J. R. Sosa-Acosta, J. A. Silva, L. Fernández-Izquierdo, S. Díaz-Castañón, M. Ortiz, J. C. Zuaznabar-Gardona and A. M. Díaz-García, Iron Oxide Nanoparticles (IONPs) with Potential Applications in Plasmid DNA Isolation, *Colloids Surf., A*, 2018, **545**, 167–178, DOI: 10.1016/j.colsurfa.2018.02.062.

25 H. H. P. Yiu, L. Bouffier, P. Boldrin, J. Long, J. B. Claridge and M. J. Rosseinsky, Comprehensive Study of DNA Binding on Iron(II,III) Oxide Nanoparticles with a Positively Charged Polyamine Three-Dimensional Coating, *Langmuir*, 2013, **29**(36), 11354–11365, DOI: 10.1021/la400848r.

26 B. Liu and J. Liu, DNA Adsorption by Magnetic Iron Oxide Nanoparticles and Its Application for Arsenate Detection, *Chem. Commun.*, 2014, **50**(62), 8568, DOI: 10.1039/C4CC03264K.

27 Chapter 4. Quantification of Total DNA by Spectroscopy, in *Analytical Molecular Biology*, ed. Parkes, H., Saunders, V. and Bedson, P., Royal Society of Chemistry, Cambridge, 2007, pp. 47–57, DOI: 10.1039/9781847559296-00047.

28 A. O. Nwokeoji, P. M. Kilby, D. E. Portwood and M. J. Dickman, Accurate Quantification of Nucleic Acids Using Hypochromicity Measurements in Conjunction with UV Spectrophotometry, *Anal. Chem.*, 2017, **89**(24), 13567–13574, DOI: 10.1021/acs.analchem.7b04000.

29 M. J. Cavaluzzi and P. N. Borer, Revised UV Extinction Coefficients for Nucleoside-5′-Monophosphates and Unpaired DNA and RNA, *Nucleic Acids Res.*, 2004, **32**(1), e13, DOI: 10.1093/nar/gnh015.

30 M. Zarei, E. K. Goharshadi, H. Ahmadzadeh and S. Samiee, Improvement of Heat Dissipation in Agarose Gel Electrophoresis by Metal Oxide Nanoparticles, *RSC Adv.*, 2015, **5**(108), 88655–88665, DOI: 10.1039/C5RA19678G.

31 P. H. Johnson and L. I. Grossman, Electrophoresis of DNA in Agarose Gels. Optimizing Separations of Conformational Isomers of Double- and Single-Stranded DNAs, *Biochemistry*, 1977, **16**(19), 4217–4225, DOI: 10.1021/bi00638a014.

32 L. L. Fernández, M. Montes-Bayón, E. B. González, L. M. Sierra, A. Sanz-Medel and J. Bettmer, Initial Studies on Quantitative DNA Induced Oxidation by Gel Electrophoresis (GE)-ICP-MS, *J. Anal. At. Spectrom.*, 2011, **26**(1), 195–200, DOI: 10.1039/C0JA00163E.

33 S. Fujii, K. Inagaki, S. Miyashita, K. Nagasawa, K. Chiba and A. A. Takatsu, Coupling System of Capillary Gel Electrophoresis with Inductively Coupled Plasma-Mass Spectrometry for the Determination of Double Stranded DNA Fragments, *Metallomics*, 2013, **5**(5), 424, DOI: 10.1039/c3mt00057e.

34 M. Sidstedt, E. L. Romsos, R. Hedell, R. Ansell, C. R. Steffen, P. M. Vallone, P. Rådström and J. Hedman, Accurate Digital Polymerase Chain Reaction Quantification of Challenging Samples Applying Inhibitor-Tolerant DNA Polymerases, *Anal. Chem.*, 2017, **89**(3), 1642–1649, DOI: 10.1021/acs.analchem.6b03746.

35 R. Sanders, J. F. Huggett, C. A. Bushell, S. Cowen, D. J. Scott and C. A. Foy, Evaluation of Digital PCR for Absolute DNA Quantification, *Anal. Chem.*, 2011, **83**(17), 6474–6484, DOI: 10.1021/ac103230c.

36 F. Cheng, Characterization of Aqueous Dispersions of Fe3O4 Nanoparticles and Their Biomedical Applications, *Biomaterials*, 2005, **26**(7), 729–738, DOI: 10.1016/j.biomaterials.2004.03.016.

37 C. Hammond, *The Basics of Crystallography and Diffraction*, International Union of Crystallography Texts on Crystallography, Oxford University Press, Oxford, 4th edn, 2015.

38 K. R. Lenhardt, H. Breitzke, G. Buntkowsky, E. Reimhult, M. Willinger and T. Rennert, Synthesis of Short-Range Ordered Aluminosilicates at Ambient Conditions, *Sci. Rep.*, 2021, **11**(1), 4207, DOI: 10.1038/s41598-021-83643-w.

39 H. Sanaeishoar, M. Sabbaghan and F. Mohave, Synthesis and Characterization of Micro-Mesoporous MCM-41 Using Various Ionic Liquids as Co-Templates, *Microporous Mesoporous Mater.*, 2015, **217**, 219–224, DOI: 10.1016/j.micromeso.2015.06.027.

40 J. Ibarra, J. Melendres, M. Almada, M. G. Burboa, P. Taboada, J. Juárez and M. A. Valdez, Synthesis and Characterization of Magnetite/PLGA/Chitosan Nanoparticles, *Mater. Res. Express*, 2015, **2**(9), 095010, DOI: 10.1088/2053-1591/2/9/095010.

41 H. Helendra, N. I. Istiqomah, H. Sabarman and E. Suharyadi, Synthesis of Varied Oleic Acid-Coated Fe3O4 Nanoparticles Using the Co-Precipitation Technique for Biosensor Applications, *Sens. Int.*, 2025, **6**, 100295, DOI: 10.1016/j.sintl.2024.100295.

42 H. Rajbongshi, A. Sarkar, P. Phukan, S. Bhattacharjee and P. Datta, Ultrasensitive Fluorescence Detection of Fe3+ Ions Using Fluorescein Isothiocyanate Functionalized Ag/SiO2/SiO2 Core–Shell Nanocomposites, *J. Mater. Sci. Mater. Electron.*, 2019, **30**(6), 5580–5597, DOI: 10.1007/s10854-019-00852-w.

43 Y.-K. Peng, C. N. P. Lui, T.-H. Lin, C. Chang, P.-T. Chou, K. K. L. Yung and S. C. E. Tsang, Multifunctional Silica-Coated Iron Oxide Nanoparticles: A Facile Four-in-One System for in Situ Study of Neural Stem Cell Harvesting, *Faraday Discuss.*, 2014, **175**, 13–26, DOI: 10.1039/C4FD00132J.

44 P. M. Nowak and M. Woźniakiewicz, The Acid-Base/Deprotonation Equilibrium Can Be Studied with a MicroScale Thermophoresis (MST), *Molecules*, 2022, **27**(3), 685, DOI: 10.3390/molecules27030685.

45 T. Kubo, S. Arimura, T. Naito, T. Sano and K. Otsuka, Competitive ELISA-like Label-Free Detection of Lysozyme by Using a Fluorescent Monomer-Doped Molecularly Imprinted Hydrogel, *Anal. Sci.*, 2017, **33**(11), 1311–1315, DOI: 10.2116/analsci.33.1311.

46 Y. Yang, M. Xia, H. Zhao, S. Zhang and X. Zhang, A Cell-Surface-Specific Ratiometric Fluorescent Probe for Extracellular pH Sensing with Solid-State Fluorophore, *ACS Sens.*, 2018, **3**(11), 2278–2285, DOI: 10.1021/acssensors.8b00514.

47 L. Ma, B. Liu, P.-J. J. Huang, X. Zhang and J. Liu, DNA Adsorption by ZnO Nanoparticles near Its Solubility Limit: Implications for DNA Fluorescence Quenching and DNAzyme Activity Assays, *Langmuir*, 2016, **32**(22), 5672–5680, DOI: 10.1021/acs.langmuir.6b00906.

48 A. Lopez and J. Liu, Fluorescence Polarization for Probing DNA Adsorption by Nanomaterials and Fluorophore/DNA Interactions, *Langmuir*, 2019, **35**(30), 9954–9961, DOI: 10.1021/acs.langmuir.9b01678.

49 W. Thongyod, C. Buranachai, T. Pengpan and C. Punwong, Fluorescence Quenching by Photoinduced Electron Transfer between 7-Methoxycoumarin and Guanine Base Facilitated by Hydrogen Bonds: An *in Silico* Study, *Phys. Chem. Chem. Phys.*, 2019, **21**(29), 16258–16269, DOI: 10.1039/C9CP02037C.

50 C. A. M. Seidel, A. Schulz and M. H. M. Sauer, Nucleobase-Specific Quenching of Fluorescent Dyes. 1. Nucleobase One-Electron Redox Potentials and Their Correlation with Static and Dynamic Quenching Efficiencies, *J. Phys. Chem.*, 1996, **100**(13), 5541–5553, DOI: 10.1021/jp951507c.

51 T. Heinlein, J.-P. Knemeyer, O. Piestert and M. Sauer, Photoinduced Electron Transfer between Fluorescent Dyes and Guanosine Residues in DNA-Hairpins, *J. Phys. Chem. B*, 2003, **107**(31), 7957–7964, DOI: 10.1021/jp0348068.

52 I. Langmuir, THE ADSORPTION OF GASES ON PLANE SURFACES OF GLASS, MICA AND PLATINUM, *J. Am. Chem. Soc.*, 1918, **40**(9), 1361–1403, DOI: 10.1021/ja02242a004.

53 J. Panchompoo, L. Aldous, M. Baker, M. I. Wallace and R. G. Compton, One-Step Synthesis of Fluorescein Modified Nano-Carbon for Pd(Ii) Detection via Fluorescence Quenching, *Analyst*, 2012, **137**(9), 2054, DOI: 10.1039/c2an16261j.

54 M. Mekawy, A. Saito, H. Shimizu and T. Tominaga, Targeting of Apoptotic Cells Using Functionalized Fe2O3 Nanoparticles, *Nanomaterials*, 2015, **5**(2), 874–884, DOI: 10.3390/nano5020874.

55 T. Weitner, T. Friganović and D. Šakić, Inner Filter Effect Correction for Fluorescence Measurements in Microplates Using Variable Vertical Axis Focus, *Anal. Chem.*, 2022, **94**(19), 7107–7114, DOI: 10.1021/acs.analchem.2c01031.

56 T. T. Trang, T. T. H. Pham, N. V. Dang, P. T. Nga, M. V. Linh and X. H. Vu, Revealing the High Efficiency of Fluorescence Quenching of Rhodamine B by Triangular Silver Nanodisks Due to the Inner Filter Effect Mechanism, *RSC Adv.*, 2024, **14**(14), 9538–9546, DOI: 10.1039/D4RA00575A.

57 J. Lietard, D. Ameur and M. M. Somoza, Sequence-Dependent Quenching of Fluorescein Fluorescence on Single-Stranded and Double-Stranded DNA, *RSC Adv.*, 2022, **12**(9), 5629–5637, DOI: **10.1039/D2RA00534D**.

58 D. Markovitsi, On the Use of the Intrinsic DNA Fluorescence for Monitoring Its Damage: A Contribution from Fundamental Studies, *ACS Omega*, 2024, **9**(25), 26826–26837, DOI: **10.1021/acsomega.4c02256**.

59 M. Balcioglu, M. Rana, N. Robertson and M. V. Yigit, DNA-Length-Dependent Quenching of Fluorescently Labeled Iron Oxide Nanoparticles with Gold, Graphene Oxide and MoS_2 Nanostructures, *ACS Appl. Mater. Interfaces*, 2014, **6**(15), 12100–12110, DOI: **10.1021/am503553h**.

60 M. Sayed and H. Pal, pH-Assisted Control over the Binding and Relocation of an Acridine Guest between a Macrocyclic Nanocarrier and Natural DNA, *Phys. Chem. Chem. Phys.*, 2015, **17**(14), 9519–9532, DOI: **10.1039/C4CP05335D**.

61 H. Schmidt-Böcking, K. Reich, A. Templeton, W. Trageser and V. Vill, S10, in *Otto Sterns Veröffentlichungen – Band 2*, ed. Schmidt-Böcking, H., Reich, K., Templeton, A., Trageser, W. and Vill, V., Springer, Berlin, Heidelberg, 2016, pp. 79–85, DOI: **10.1007/978-3-662-46962-0_5**.

62 J. Keizer, Nonlinear Fluorescence Quenching and the Origin of Positive Curvature in Stern-Volmer Plots, *J. Am. Chem. Soc.*, 1983, **105**(6), 1494–1498, DOI: **10.1021/ja00344a013**.

63 V. V. Koppal, R. Melavanki, R. Kusanur, Z. K. Bagewadi, D. A. Yaraguppi, S. H. Deshpande and N. R. Patil, Investigation of the Fluorescence Turn-off Mechanism, Genome, Molecular Docking *In Silico* and *In Vitro* Studies of 2-Acetyl-3 *H* -Benzo[*f*]Chromen-3-One, *ACS Omega*, 2022, **7**(27), 23759–23770, DOI: **10.1021/acsomega.2c02424**.

64 H. L. Ding, Y. X. Zhang, S. Wang, J. M. Xu, S. C. Xu and G. H. Li, Fe_3 O_4 @SiO_2 Core/Shell Nanoparticles: The Silica Coating Regulations with a Single Core for Different Core Sizes and Shell Thicknesses, *Chem. Mater.*, 2012, **24**(23), 4572–4580, DOI: **10.1021/cm302828d**.